AIAA JOURNAL
Vol. 45, No. 2, February 2007

Large-Eddy Simulation of Compressible Transitional Flows in a Low-Pressure Turbine Cascade

Kazuo Matsuura*
Kyushu University, Fukuoka 819-0395, Japan
and
Chisachi Kato†
University of Tokyo, Tokyo 153-8505, Japan

DOI: 10.2514/1.22425

Large-eddy simulation of compressible transitional flows in a low-pressure turbine cascade is performed by using sixth-order compact difference and a 10th-order filtering method. Numerical results without freestream turbulence and those with about 5% of freestream turbulence are compared. In these simulations, separated flows in the turbine cascade accompanied by laminar-turbulent transition are realized, and the present results closely agree with past experimental measurements in terms of the static pressure distribution around the blade. In the case where no freestream turbulence is taken into account, the unsteady pressure field essentially differs from that with strong freestream turbulence. In the no freestream turbulence case, pressure waves that propagate from the blade's wake region have noticeable effects on the separated-boundary layer near the trailing edge and on the neighboring blade. Also, based on the snapshot proper orthogonal decomposition analysis, dominant behaviors of the transitional boundary layers are investigated.

Nomenclature

C	=	chord length
C_f	=	friction coefficient
C_p	=	pressure coefficient
c	=	speed of sound
d	=	distance from a grid point to a wall
e	=	total energy per unit mass
$E(k)$	=	energy spectrum
$\boldsymbol{F}, \boldsymbol{G}, \boldsymbol{H}$	=	inviscid flux vectors
$\boldsymbol{F}_v, \boldsymbol{G}_v, \boldsymbol{H}_v$	=	viscous flux vectors
G	=	convolution kernel of grid filter
H	=	shape factor
J	=	Jacobian
k	=	wave number
L	=	length
l	=	cascade pitch
M_a	=	Mach number
P_k	=	turbulent production
P_r	=	Prandtl number
P_t	=	total pressure
p	=	static pressure
$\boldsymbol{Q}$	=	conservative variables
Q_i	=	heat flux
q_i	=	subgrid-scale heat flux
R	=	gas constant
Re	=	Reynolds number
R_1, R_2	=	Riemann invariant
$\boldsymbol{S}$	=	source-term vector
T	=	temperature
Tu	=	turbulence intensity
t	=	time
U_1, U_2, U_3	=	contravariant velocity components
u_1, u_2, u_3	=	velocity components in Cartesian coordinates
u_ξ	=	streamwise velocity component
w	=	velocity
$x, y, z; x_1, x_2, x_3$	=	Cartesian coordinates
α_f	=	filter parameter
β	=	flow angle
γ	=	specific heat ratio
Δt	=	time increment
δ	=	boundary layer thickness
δ_{ij}	=	Kronecker's delta function
δ^*	=	displacement thickness
Λ_f	=	longitudinal integral scale
λ	=	thermal conductivity
μ	=	molecular viscosity
$\xi, \eta, \zeta, \xi_1, \xi_2, \xi_3$	=	general curvilinear coordinates
$\xi_t, \xi_x, \xi_y, \xi_z, \eta_t, \eta_x, \eta_y, \eta_z, \zeta_t, \zeta_x, \zeta_y, \zeta_z$	=	metrics
ρ	=	density
σ_{ij}	=	viscous stress tensor
τ_{ij}	=	subgrid-scale stress tensor
Ω	=	entire computational domain
ω	=	vorticity magnitude
$\partial_\xi, \partial_\eta, \partial_\zeta$	=	differential operator

Subscripts

B	=	extrapolated value from the interior of the computational domain
min	=	minimum
rms	=	root mean square
th	=	theoretical isentropic flow
w	=	wall
$1, 2, \infty$	=	cascade conditions: inlet, outlet, freestream
$\perp$	=	perpendicular to inlet boundary
$\parallel$	=	parallel to inlet boundary

Superscripts

t	=	transpose
$\bar{\ }$	=	grid-filtered quantity

Received 18 January 2006; revision received 11 July 2006; accepted for publication 25 October 2006.

*Postdoctral Researcher, Department of Intelligent Machinery and Systems, Faculty of Engineering, 744 Motooka, Nishi-ku, Fukuoka-shi; kazuo@mech.kyushu-u.ac.jp.

†Professor, Institute of Industrial Science, The 2nd Department, 4-6-1 Komaba, Meguro-ku; ckato@iis.u-tokyo.ac.jp.

$'$ = deviation from grid-filtered average
$''$ = deviation from Reynolds-averaged quantity
$\tilde{}$ = Favre-filtered quantity
$\hat{}$ = compact filtering
$+$ = wall unit

I. Introduction

THE aerodynamic performance of a cascade has a great influence on the energy conversion efficiency in aeronautical as well as industrial gas turbines, which has prompted extensive research on cascade flows. In particular, accurate prediction of and detailed investigation into compressible low-Reynolds number cascade flows are crucial to improve the efficiency of aeronautical low-pressure turbines that operate at 2–5% below the designed efficiency at altitude [1], or to reduce the loss in industrial small-sized turbines that increases with decreasing Reynolds number at its -0.20– -0.85th power [2], and therefore, further research on low-Reynolds number cascade flows seems necessary.

In low-pressure turbines or small-sized turbines, the Reynolds number based on the chord length and the throat exit velocity becomes as small as on the order of 10^4–10^5 due to a decrease in density, resulting in an increase in kinematic viscosity or due to the small length scale. The boundary layer on the blade in such a turbine thus becomes transitional and unsteadiness of the cascade flows becomes evident. At the same time, the boundary layers are affected by the strong freestream turbulence with about 5–20% intensity that originates in the combustion chamber or wakes of the upstream blade rows.

Conventionally, the Reynolds-averaged Navier–Stokes simulation (RANS) has been widely used for the prediction of transitional flows. In this method, transition is treated empirically, for example, by correlating the transition point or transition length with the momentum thickness of the boundary layer, or by assuming a production rate of turbulent spots based on Emmons's spot theory [3]. However, the transition location or the spot production rate is usually estimated from limited and scattered experimental data. Therefore, the accuracy of the prediction deteriorates when it is applied to those operating conditions that are beyond the assumptions of the empirical transition treatments, and/or to three-dimensional complex shapes.

Recently, numerical methods that solve the Navier–Stokes equation as directly as possible have been developed and applied to the prediction of transitional flows. These methods are capable of directly treating the temporal evolution of flow disturbances and frequency contents of freestream disturbances that are vital in the transitional processes. Among these methods, large-eddy simulation (LES) can predict turbulent flows with reasonable accuracy at a smaller computational cost than is needed for direct numerical simulation (DNS) and therefore, its applications are expected to spread to a wide range of engineering flows.

DNS and LES of transitional flows in a low-pressure turbine were performed by several researchers [4–10], and physical aspects of the flows have been revealed gradually. Concerning the computations without freestream turbulence, Mittal et al. [4] conducted LES of a low-pressure turbine with Reynolds numbers of $O(10^4)$ and analyzed the process of unsteady separation of the boundary layer. Based on the results, they stated that the separation of the boundary layer on the suction surface is strongly affected by the behavior of Kármán vortices near the trailing edge in their computation for Reynolds number of 1.4×10^4, and that the separated shear layer is mainly affected by the Kelvin–Helmholtz instability for a higher Reynolds number. Raverdy et al. [5] calculated transitional separated flows in a cascade with Reynolds number of 1.6×10^5 by a compressible numerical method where LES is coupled with a two-dimensional computation. They analyzed the transition process focusing on the unsteady characteristics of the laminar separation bubble and reported the existence of coupling between the separation bubble and the vortex shedding from the trailing edge.

Concerning the computations with freestream turbulence, Wu and Durbin [6] conducted DNS on bypass transition caused by the influences of periodic upstream wakes. They investigated the process of turbulent spot production due to the interaction of the wakes with the blade boundary layer and the vortical structures that are created by the passage of wakes in a cascade. Kalitzin et al. [7] investigated the effects of different types of inlet disturbances on the boundary layer transition near a blade surface. For a turbulence-free inlet condition, natural transition occurs near the trailing edge on the suction side of the blade. For grid turbulence and wake inlet conditions, bypass transition occurs further upstream, triggered by the convection of the inlet disturbances to the boundary layer of the blade.

In the studies mentioned above [4–10], unsteady behaviors of a separation bubble near the trailing edge of a low-pressure turbine have been investigated in detail in relation with no freestream turbulence case. Regarding the freestream turbulence case, the changes in the transition mode of a cascade for different types of freestream turbulence are investigated.

However, it is not thoroughly understood what would result from the unsteady behaviors near the trailing edge in the cascade passages, or how unsteady separation and/or boundary layer transition in a low-pressure turbine changes according to the change in freestream turbulence. Investigation into these issues is important not only for predicting transitional boundary layers accurately but also for understanding the mechanism of noise generation from an aeroacoustical point of view.

In this paper, large-eddy simulations of a low-pressure turbine cascade flow subjected to freestream turbulence are performed. Based on the computed results, detailed investigations are presented on the effects of the freestream turbulence on the boundary layer transition and the behavior of the pressure waves that originate near the trailing edge with its effects on the separation/transition of the boundary layer [10]. Also presented in this paper are the dominant unsteady behaviors in the transitional boundary layers that are extracted by snapshot proper orthogonal decomposition (POD) analysis [11].

II. Governing Equations and Numerical Methods

A. Governing Equations

The governing equations are the unsteady three-dimensional compressible Favre-filtered Navier–Stokes equations, written in conservative variables and expressed notationally in the following form:

$$\frac{\partial \boldsymbol{Q}}{\partial t} + \frac{\partial}{\partial \xi}(\boldsymbol{F} - \boldsymbol{F}_v) + \frac{\partial}{\partial \eta}(\boldsymbol{G} - \boldsymbol{G}_v) + \frac{\partial}{\partial \varsigma}(\boldsymbol{H} - \boldsymbol{H}_v) = \boldsymbol{S} \tag{1}$$

To derive the governing equations for LES, an arbitrary variable is filter averaged as

$$\bar{f} = \int_\Omega G f \, \mathrm{d}\Omega \tag{2}$$

where G is the kernel of the grid filtering and the integration is carried out over the entire computational domain Ω. This allows f to be decomposed into its grid-scale (GS) $\bar{f}$ and subgrid-scale (SGS) f' components.

$$f = \bar{f} + f' \tag{3}$$

In compressible flows, the grid-scale quantity is recast in terms of a Favre-filtered variable:

$$\tilde{f} = \frac{\overline{\rho f}}{\bar{\rho}} \tag{4}$$

Based on the average defined above, the vector of conservative variables is given as

$$\boldsymbol{Q} = \frac{1}{J}(\bar{\rho}, \bar{\rho}\tilde{u}_1, \bar{\rho}\tilde{u}_2, \bar{\rho}\tilde{u}_3, \bar{\rho}\,\tilde{e})^t \tag{5}$$

and the inviscid and viscous vector fluxes [12]

$$\boldsymbol{F} = \frac{1}{J}\begin{bmatrix} \bar{\rho}\tilde{U}_1 \\ \bar{\rho}\tilde{u}_1\tilde{U}_1 + \xi_x\bar{p} \\ \bar{\rho}\tilde{u}_2\tilde{U}_1 + \xi_y\bar{p} \\ \bar{\rho}\tilde{u}_3\tilde{U}_1 + \xi_z\bar{p} \\ \bar{\rho}\,\tilde{e}\,\tilde{U}_1 + \xi_{x_i}\tilde{u}_i\bar{p} \end{bmatrix}, \qquad \boldsymbol{G} = \frac{1}{J}\begin{bmatrix} \bar{\rho}\tilde{U}_2 \\ \bar{\rho}\tilde{u}_1\tilde{U}_2 + \eta_x\bar{p} \\ \bar{\rho}\tilde{u}_2\tilde{U}_2 + \eta_y\bar{p} \\ \bar{\rho}\tilde{u}_3\tilde{U}_2 + \eta_z\bar{p} \\ \bar{\rho}\,\tilde{e}\,\tilde{U}_2 + \eta_{x_i}\tilde{u}_i\bar{p} \end{bmatrix}$$

$$\boldsymbol{H} = \frac{1}{J}\begin{bmatrix} \bar{\rho}\tilde{U}_3 \\ \bar{\rho}\tilde{u}_1\tilde{U}_3 + \zeta_x\bar{p} \\ \bar{\rho}\tilde{u}_2\tilde{U}_3 + \zeta_y\bar{p} \\ \bar{\rho}\tilde{u}_3\tilde{U}_3 + \zeta_z\bar{p} \\ \bar{\rho}\,\tilde{e}\,\tilde{U}_3 + \zeta_{x_i}\tilde{u}_i\bar{p} \end{bmatrix} \tag{6}$$

$$\boldsymbol{F}_v = \frac{1}{J}\begin{bmatrix} 0 \\ \xi_{x_i}(\tilde{\sigma}_{i1} - \tau_{i1} + A_{i1}) \\ \xi_{x_i}(\tilde{\sigma}_{i2} - \tau_{i2} + A_{i2}) \\ \xi_{x_i}(\tilde{\sigma}_{i3} - \tau_{i3} + A_{i3}) \\ \xi_{x_i}[\tilde{u}_j(\tilde{\sigma}_{ij} - \tau_{ij}) - q_i - \tilde{Q}_i + B_{1i} - B_{2i}] \end{bmatrix}$$

$$\boldsymbol{G}_v = \frac{1}{J}\begin{bmatrix} 0 \\ \eta_{x_i}(\tilde{\sigma}_{i1} - \tau_{i1} + A_{i1}) \\ \eta_{x_i}(\tilde{\sigma}_{i2} - \tau_{i2} + A_{i2}) \\ \eta_{x_i}(\tilde{\sigma}_{i3} - \tau_{i3} + A_{i3}) \\ \eta_{x_i}[\tilde{u}_j(\tilde{\sigma}_{ij} - \tau_{ij}) - q_i - \tilde{Q}_i + B_{1i} - B_{2i}] \end{bmatrix} \tag{7}$$

$$\boldsymbol{H}_v = \frac{1}{J}\begin{bmatrix} 0 \\ \zeta_{x_i}(\tilde{\sigma}_{i1} - \tau_{i1} + A_{i1}) \\ \zeta_{x_i}(\tilde{\sigma}_{i2} - \tau_{i2} + A_{i2}) \\ \zeta_{x_i}(\tilde{\sigma}_{i3} - \tau_{i3} + A_{i3}) \\ \zeta_{x_i}[\tilde{u}_j(\tilde{\sigma}_{ij} - \tau_{ij}) - q_i - \tilde{Q}_i + B_{1i} - B_{2i}] \end{bmatrix}$$

$$\boldsymbol{S} = \frac{1}{J}\begin{bmatrix} 0 \\ 0 \\ 0 \\ 0 \\ -B_3 + B_4 + B_5 \end{bmatrix}$$

where

$$\begin{aligned} \tilde{U}_1 &= \xi_t + \xi_x\tilde{u}_1 + \xi_y\tilde{u}_2 + \xi_z\tilde{u}_3 \\ \tilde{U}_2 &= \eta_t + \eta_x\tilde{u}_1 + \eta_y\tilde{u}_2 + \eta_z\tilde{u}_3 \\ \tilde{U}_3 &= \zeta_t + \zeta_x\tilde{u}_1 + \zeta_y\tilde{u}_2 + \zeta_z\tilde{u}_3 \end{aligned} \tag{8}$$

$$\bar{\rho}\,\tilde{e} = \frac{\bar{p}}{(\gamma - 1)} + \frac{1}{2}\bar{\rho}(\tilde{u}_1^2 + \tilde{u}_2^2 + \tilde{u}_3^2)$$

Components of the viscous stress tensor and heat flux vector are expressed as

$$\bar{\sigma}_{ij} = \mu(\tilde{T})\left(\frac{\partial\xi_k}{\partial x_j}\frac{\partial\tilde{u}_i}{\partial\xi_k} + \frac{\partial\xi_k}{\partial x_i}\frac{\partial\tilde{u}_j}{\partial\xi_k} - \frac{2}{3}\delta_{ij}\frac{\partial\xi_l}{\partial x_k}\frac{\partial\tilde{u}_k}{\partial\xi_l}\right) \tag{9}$$

$$\tilde{Q}_i = -\lambda\frac{\partial\xi_j}{\partial x_i}\frac{\partial\tilde{T}}{\partial\xi_j} \tag{10}$$

while the corresponding SGS stress and SGS heat flux are provided by

$$\tau_{ij} = -\bar{\rho}\tilde{u}_i\tilde{u}_j + \overline{\rho u_i u_j} \tag{11}$$

$$q_i = \frac{R}{\gamma - 1}(-\bar{\rho}\tilde{u}_i\tilde{T} + \overline{\rho u_i T}) \tag{12}$$

Other subgrid terms read

$$A_{ij} = \bar{\sigma}_{ij} - \tilde{\sigma}_{ij} \tag{13}$$

$$B_{1j} = \bar{\sigma}_{jk}\tilde{u}_k - \tilde{\sigma}_{jk}\tilde{u}_k \tag{14}$$

$$B_{2j} = \bar{Q}_j - \tilde{Q}_j \tag{15}$$

$$B_3 = \overline{p\frac{\partial u_j}{\partial\xi_k}\frac{\partial\xi_k}{\partial x_j}} - \bar{p}\frac{\partial\tilde{u}_j}{\partial\xi_k}\frac{\partial\xi_k}{\partial x_j} \tag{16}$$

$$B_4 = \tau_{kj}\frac{\partial\tilde{u}_k}{\partial\xi_i}\frac{\partial\xi_i}{\partial x_j} \tag{17}$$

$$B_5 = \overline{\sigma_{jk}\frac{\partial u_k}{\partial\xi_i}\frac{\partial\xi_i}{\partial x_j}} - \bar{\sigma}_{jk}\frac{\partial\tilde{u}_k}{\partial\xi_i}\frac{\partial\xi_i}{\partial x_j} \tag{18}$$

The perfect gas law closes the system of equations.

$$\bar{p} = \bar{\rho}R\tilde{T} \tag{19}$$

Sutherland's formula for viscosity is adopted and a constant Prandtl number $Pr = 0.72$ is assumed.

In this study, it is assumed that

$$\overline{\mu(T)S_{ij}} \cong \mu(\tilde{T})\tilde{S}_{ij} \tag{20}$$

where $S_{ij} = (\partial u_i/\partial x_j + \partial u_j/\partial x_i)/2$ is the strain-rate tensor, and an equivalent equality involving the thermal conductivity applies based on the a priori study by Vreman et al. [13] Therefore, $A_{ij} = B_{1j} = B_{2j} = 0$. B_5 is also neglected.

SGS models that incorporate the effects of SGS stress and SGS heat flux on the GS flow have been proposed by many researchers for compressible flows [14–18]. These models are categorized into explicit models and implicit ones. In the former, τ_{ij} and q_i are evaluated by the GS variables and introduced in the basic equations to close the system. In the latter, the effects of SGS eddies on the GS variables are implicitly included in the numerical schemes based on the energy transfer between the GS and SGS eddies.

Among the former models, the Smagorinsky model [15,19] and the dynamic model [16,20], that determines its model coefficient based on the information of the flowfields near the grid cutoff scale, have been mainly used for practical applications. The Smagorinsky model assumes turbulent production everywhere there is velocity gradient, and the SGS eddy viscosity is decreased by using Van Driest's dumping function [21] or a dynamic procedure near wall surfaces [20]. Although these eddy viscosity models are generally based on the equilibrium hypothesis that turbulence production equals turbulence dissipation, prediction capability of these models, in general, deteriorates in the viscous sublayer and transitional boundary layers where this hypothesis does not hold.

On the other hand, it has been reported that the numerical dissipation that is inherent in numerical schemes plays equivalent roles to an SGS model if it is introduced properly for high-resolution

computations [17]. It has also been reported that by applying a low-pass filter that dumps out those fluctuations with a high wave number, better results can be obtained than computations with the standard Smagorinsky model or the dynamic Smagorinsky model [18].

Therefore, in the present study, no explicit SGS model is used, that is, $\tau_{ij} = 0$, $q_i = 0$. Here, effect of the pressure dilatation B_3 is also neglected because the present study deals with shock-free cases only. Instead, the energy in the GS transferred to the SGS eddies is dissipated by the 10th-order spatial filter, mentioned later, that removes numerical instabilities at the same time.

B. Numerical Methods

The equations are solved by the finite-difference method. Spatial derivatives that appear in metrics, convective, and viscous terms are evaluated by the sixth-order tridiagonal compact scheme [22]:

$$\frac{1}{3}\left.\frac{\partial f}{\partial \xi}\right|_{i-1} + \left.\frac{\partial f}{\partial \xi}\right|_{i} + \frac{1}{3}\left.\frac{\partial f}{\partial \xi}\right|_{i+1} = \frac{1}{36}(f_{i+2} - f_{i-2}) + \frac{7}{9}(f_{i+1} - f_{i-1}), \qquad i \in \{3, \ldots, i\max - 2\} \tag{21}$$

Near boundaries, the fourth-order one-sided compact scheme [22] is used at boundary points and the fourth-order classical Padé scheme is used at one point interior from boundaries.

Time-accurate solutions to the governing equations were obtained by the implicit approximately factored finite-difference algorithm of Beam and Warming [23] based on the three-point-backward formulation. In the present method, the computational efficiency is improved by adopting Pulliam and Chaussee's diagonalization [24]. To increase the convergence of the method, fourth-order artificial dissipation [25] is added to each factor. Three Newton-like subiterations per time step are employed to reduce errors induced by linearization, factorization, and diagonalization. By the iterations, the residual, that is, the right-hand side of the Δ-form equation [23] decreases by third order of magnitude. The final accuracy of the time integration is of second order.

In addition to the above-mentioned spatial discretization and time integration, a filtering operation is introduced as an implicit SGS model suppressing the physically generated small eddies and to suppress nonphysical numerical instabilities which originate in the linear instability of the scheme [26] and the boundary extrapolation used later, or the curvature of the grid. For incompressible flow simulations, a transformation of the convective terms or a staggered grid is used to suppress the numerical instabilities [27]. However, for simulations of compressible flows such as in a turbine cascade, the calculation is sensitive to the numerical instabilities even at subsonic conditions. As a result, some stabilization procedure is inevitably needed from an engineering point of view. Therefore, the 10th-order implicit filter shown below [28] is used.

$$\alpha_f \hat{\phi}_{i-1} + \hat{\phi}_i + \alpha_f \hat{\phi}_{i+1} = \sum_{n=0}^{5} \frac{a_n}{2}(\phi_{i+n} + \phi_{i-n}), \qquad i \in \{6, \ldots, i\max - 5\} \tag{22}$$

Here, ϕ denotes a conservative quantity and $\hat{\phi}$ a filtered quantity at each grid point. Regarding coefficients a_n $(n = 0, \ldots, 5)$, the values in [28] repeated in Table 1 are used in the present study. The parameter α_f is set to be 0.46. Near boundaries, an implicit filter of a decreased order, that is, second order for $i = 2$ and $i\max - 1$, fourth order for $i = 3$ and $i\max - 2$, sixth order for $i = 4$ and $i\max - 3$, and eighth order for $i = 5$ and $i\max - 4$, is used.

Not only the accuracy of the filter but also the value of α_f has a considerable influence both on the accuracy and on the stability of the calculation. In the present study, the above value is used to keep the stability of the calculation while maintaining high accuracy of the computational results. As described later in Sec. II.C, the above method is validated for the prediction of bypass transition on a flat plate [29].

To run the program that implements the numerical methods mentioned previously on a distributed-memory parallel computer, the program is parallelized using the message passing interface (MPI). In this process, it is necessary to parallelize the tridiagonal matrices that appear in the compact schemes, and pentadiagonal matrices that appear in the time integration because of the usage of the fourth-order artificial dissipation. Usually, to minimize overhead due to interprocess communications, sweep is performed only within each process and data are exchanged with the neighboring processes by overlapping a few grid points. However, when such a method was used strong filtering was needed to keep computational stability, and as a result, the resolution of the calculation in the entire region was degraded severely. Therefore, in the present study, a pipelining algorithm [30], in which sweep is performed over all the processes in each direction, is adopted for solving the band matrices.

C. Validation

To validate the effectiveness of the present numerical method, simulations of bypass transition on a flat plate are performed [29], and the numerical results are compared with experimental data [31]. Bypass transition is known as the most typical mode of transition in gas turbine cascade flows.

In the numerical method, the value of parameter α_f, that is the amount of artificial dissipation, generally plays a critical role in determining the accuracy of computational results. Therefore, the effect of the filter parameter is discussed. Also, the effect of introducing an additional explicit SGS model to the present method is discussed.

Computed flow is an almost incompressible spatially growing boundary layer on a flat plate. The freestream Mach number is 0.3 and freestream turbulence intensity is 6%. The streamwise Reynolds number Re_x of the computational domain extends from 6.625×10^3 to 4.26×10^5. Grid points used are 1134, 70, and 76, and the grid resolutions are $\Delta x^+ = 14$–38, $\Delta y^+ = 1$–76, and $\Delta z^+ = 15$ for the streamwise, wall-normal, and spanwise directions, respectively. In particular, Δx^+ is gradually decreased from 38 to 14 for $Re_x = 1.04 \times 10^5$–2.08×10^5 and gradually increased from 14 to 30 for $Re_x = 2.08 \times 10^5$–4.26×10^5. The wall units are based on the friction velocity just after transition completes.

Test cases are the computations with $\alpha_f = 0.49$ for case A, $\alpha_f = 0.45$ for case B, and $\alpha_f = 0.35$ for case C when no additional explicit SGS model is used, and $\alpha_f = 0.49$ for case D when the additional explicit SGS model [32] is used. In addition to the computations, a computation without filtering is also conducted. However, the computation diverges in this case; therefore, the results are not shown here.

Table 1 Coefficients for filter formula [28]

Order of accuracy	a_0	a_1	a_2	a_3	a_4	a_5
2	$\frac{1}{2}+\alpha_f$	$\frac{1}{2}+\alpha_f$	0	0	0	0
4	$\frac{5}{8}+\frac{3\alpha_f}{4}$	$\frac{1}{2}+\alpha_f$	$\frac{-1}{8}+\frac{\alpha_f}{4}$	0	0	0
6	$\frac{11}{16}+\frac{5\alpha_f}{8}$	$\frac{15}{32}+\frac{17\alpha_f}{16}$	$\frac{-3}{16}+\frac{3\alpha_f}{8}$	$\frac{1}{32}-\frac{\alpha_f}{16}$	0	0
8	$\frac{93+70\alpha_f}{128}$	$\frac{7+18\alpha_f}{16}$	$\frac{-7+14\alpha_f}{32}$	$\frac{1}{16}-\frac{\alpha_f}{8}$	$\frac{-1}{128}+\frac{\alpha_f}{64}$	0
10	$\frac{193+126\alpha_f}{256}$	$\frac{105+302\alpha_f}{256}$	$\frac{15(-1+2\alpha_f)}{64}$	$\frac{45(1-2\alpha_f)}{512}$	$\frac{5(-1+2\alpha_f)}{256}$	$\frac{1-2\alpha_f}{512}$

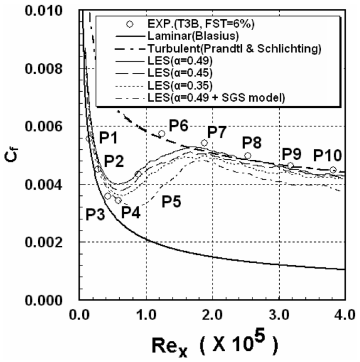

Fig. 1 Variation of skin-friction coefficient C_f with respect to Re_x.

Concerning the boundary conditions, laminar boundary layer profile subjected to isotropic freestream turbulence is imposed at the upstream boundary. The freestream turbulence is obtained from an LES result of isotropic turbulence. At the outflow boundary, a nonreflecting boundary condition [33] is used. At the upper and spanwise boundaries, symmetric and periodic boundary conditions are used, respectively. The nonslip adiabatic boundary condition is assumed at the wall boundary. The time increment was set constant at $\Delta t = 1.75 \times 10^{-5}\, L_x/u_\infty$ where L_x is the streamwise length of the computational domain and u_∞ is the freestream velocity.

The computational results of the friction coefficient C_f compared with the experimental data [31] are shown in Fig. 1. When no explicit SGS model is used, the results of cases A–C agree well with the experimental data if the region where transition completes, that is, P6 is excluded. As α_f is decreased, C_f curves shift downstream due to the artificial dissipation introduced in the calculations. In the turbulent region, the predicted C_f agrees well with the experimental data especially when $\alpha_f > 0.45$.

On the other hand, the position of maximum C_f is delayed compared to the experimental data even if α_f is taken to be as high as 0.49. Because this delay is observed independent of the values of α_f, the grid resolution, which is the other factor than filtering in determining the resolution of the computation, seems intrinsically insufficient. For comparison, the past DNS result [34] of bypass transition is shown in Fig. 2. Figure 2 shows the variation of skin-friction coefficient C_f with respect to momentum thickness Reynolds number Re_θ with freestream turbulence of 3%.

This DNS uses grid resolutions of $\Delta x^+ = 11.7$, $\Delta z^+ = 6$ with second-order central differencing for the spatial scheme. However, the position of maximum C_f ($Re_\theta \approx 350$) is delayed similar to our results. This means that even if the commonly accepted grid resolution of DNS is used, it is difficult to predict accurately rapid phenomena which occur in the region where transition completes, and this is considered to be the limitation of the state-of-the-art transition prediction. Except for this region, the present LES predicts the variation of the skin-friction coefficient with respect to the Reynolds number generally well.

When the explicit SGS model is used, transition is clearly delayed as is found in the comparison of the results of case D with those of cases A–C. This delay of transition is also confirmed by the distribution of the power spectrum density of streamwise velocity fluctuation u' at P5 and P8 as shown in Fig. 3. This suggests that the addition of the explicit SGS model to the present numerical method degrades the computational accuracy.

Figures 4–6 show streamwise velocity, streamwise velocity fluctuation, and Reynolds stress at each streamwise position, respectively. Although the growth of $u_{\rm rms}$ near the wall is underestimated compared to the experimental data at P3–P6 which correspond to transitional region, the present results of cases A–C reproduce the growth of disturbances confirmed in the experiment well.

Based on these results, the present numerical method is reasonable to be used in the present study with the grid resolution mentioned in this section and $\alpha_f > 0.45$.

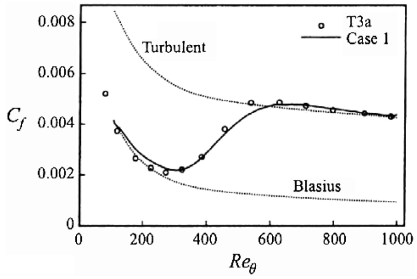

Fig. 2 Variation of skin-friction coefficient C_f with respect to momentum thickness Reynolds number Re_θ predicted by DNS for bypass transition with freestream turbulence of 3% [34].

III. Computational Details

The computational geometry is T106 [35], which is one of the most representative test cases for compressible transitional turbine cascade flows. For its design point, numerical simulations without freestream turbulence (cases A, C, and D) and that with about 5% of freestream turbulence (case B) are conducted, as shown in Table 2. Here, cases C and D are conducted to show the effect of the length of the time period for statistical average and the grid density, respectively, on the convergence of the solution in case A.

Freestream turbulence is generated by a simulation of isotropic turbulence that is conducted separately as will be described later, and the instantaneous flowfields are introduced from the inlet boundary of the computational domain of the cascade flow. The degree of inlet turbulence is defined as

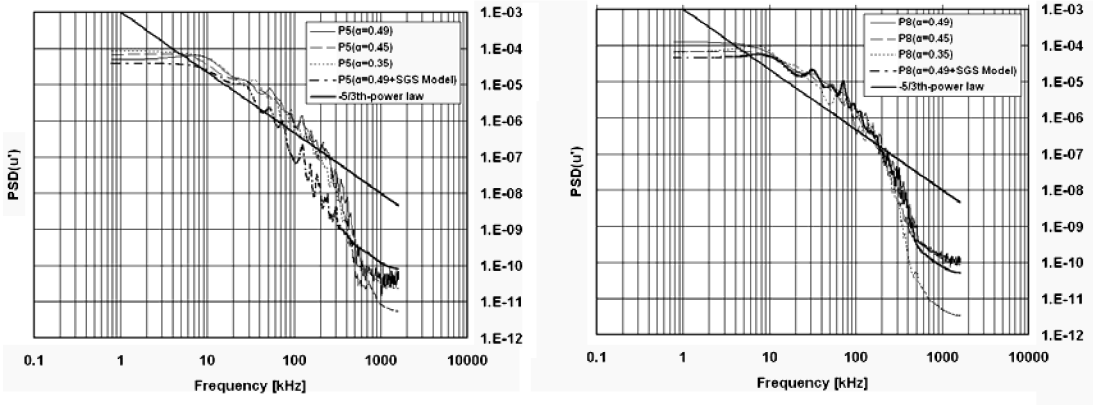

a) P5 (y/δ =0.162) **b) P8 (y/δ =0.04)**

Fig. 3 Distributions of power spectrum density of streamwise velocity fluctuation u' at P5 and P8.

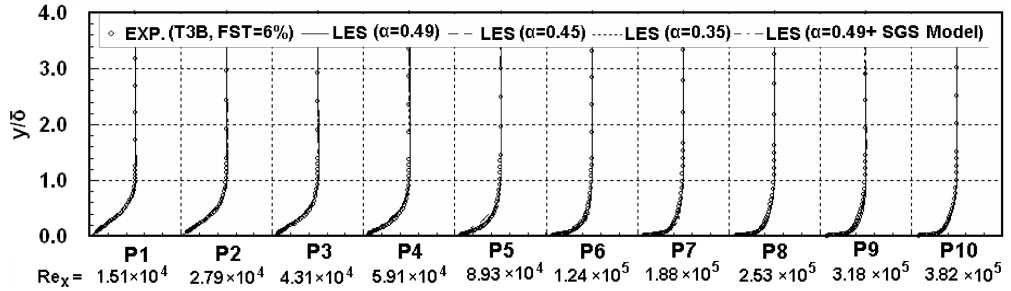

Fig. 4 Profiles of streamwise velocity at each streamwise position.

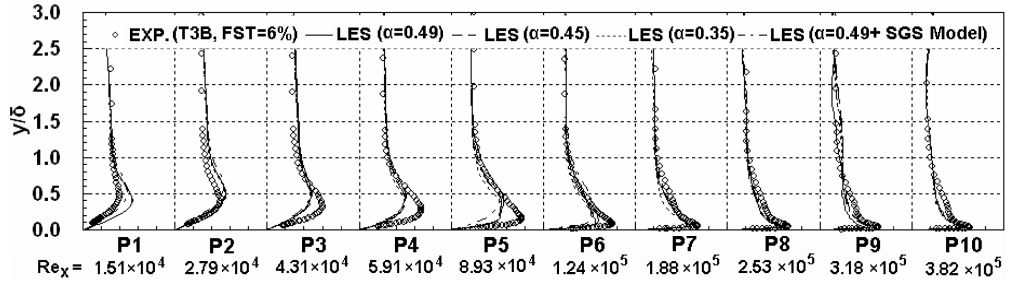

Fig. 5 Profiles of streamwise velocity fluctuation $u_{\mathrm{rms}}/u_\infty$ at each streamwise position.

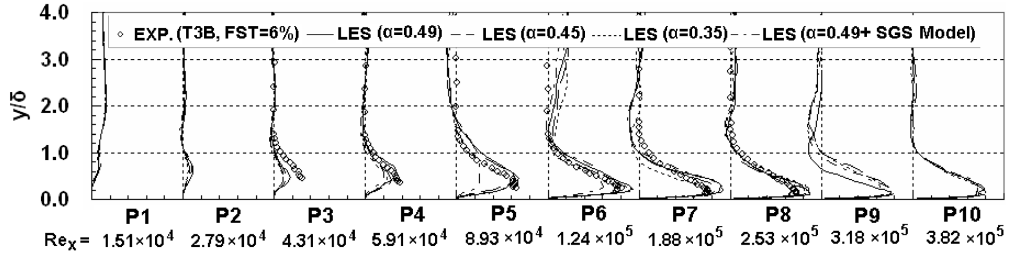

Fig. 6 Profiles of Reynolds stress $-\overline{u'v'}/u_\infty^2$ at each streamwise position.

$$Tu_1 = \frac{\sqrt{\overline{w_1''^2}}}{w_1} \tag{23}$$

where w_1'' is the fluctuating velocity component in the direction of w_1 [35].

The cascade geometry and the design data are shown in Fig. 7 and Table 3, respectively. The Mach number at the throat exit is 0.59 and the Reynolds number based on the chord length C and the throat exit velocity at the design point is 5.0×10^5. The circle that inscribes the throat contacts with the blade's suction surface at the 46.5% chord length position, as shown in Fig. 7. Fluctuations of static pressure and velocity will be discussed later for 40, 65, 75, 85, and 95% chord length positions as indicated by the arrows in the same figure. Figure 8 presents the computational grid used in the present study for cases A–C where every 10 grid lines are shown for clarity reason. The grid is of H-type topology and generated by an elliptic method in the blade passage. The inflow boundary is located at $0.5C$ upstream of the leading edge, while the outflow boundary is located at $1C$ downstream of the trailing edge. The spanwise length of the grid is 10% of the chord length that approximately corresponds to 6 times the expected distance between the adjacent low speed streaks in the turbulent boundary layer at the present Reynolds number. The adequacy of the spanwise extent of the computational domain is confirmed by checking the decay of the two-point correlations [29]. For cases A–C, the number of grid points are 1005, 150, and 40,

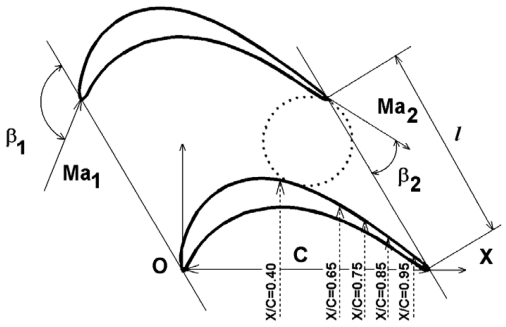

Fig. 7 Cascade geometry.

Table 2 Computational cases

Case	Tu_1	Number of grid points	Time average
A	0.0%	$1005 \times 150 \times 40$	$1\ C/w_\infty$
B	5.1%	$1005 \times 150 \times 40$	$1\ C/w_\infty$
C	0.0%	$1005 \times 150 \times 40$	$3\ C/w_\infty$
D	0.0%	$1400 \times 220 \times 159$	$1\ C/w_\infty$

Table 3 Cascade design data

Design point condition		
Isentropic outlet Mach no.	$Ma_{2,\mathrm{th}}$	0.59
Isentropic outlet Reynolds no.	$Re_{2,\mathrm{th}}$	5.0×10^5
Inlet flow angle	β_1	127.7°
Outlet flow angle	β_2	26.8°
Geometry		
Chord length	C	100 mm
Pitch/chord ratio	l/C	0.799

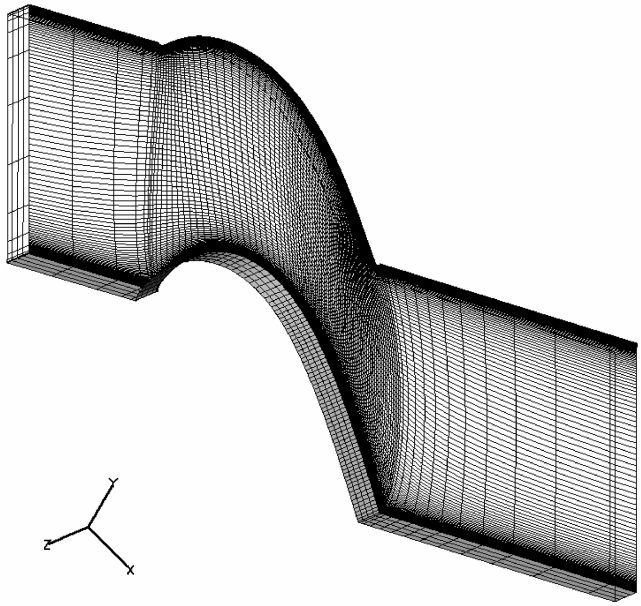

Fig. 8 Calculation grid for cases A–C (every 10 grid lines are shown).

respectively, in the streamwise, pitchwise, and spanwise directions, and approximately 6×10^6 in total. For case D, the number of grid points are 1400, 220, and 159, and approximately 49×10^6 in total.

In the former grid, the grid resolutions are $\Delta\xi^+ < 15$ and $\Delta\zeta^+ < 30$ in the streamwise and spanwise directions, respectively, near the 60–90% chord length position, and $\Delta\xi^+ < 10$ and $\Delta\zeta^+ < 20$ near the 80% chord length position where critical phenomena such as separation or transition are expected to occur. In the pitchwise direction, $\Delta\eta^+_{\min} < 2.3$ near the 60–90% chord length position and $\Delta\eta^+_{\min} < 1.0$ near the 80% chord length position. The above wall units are based on the local friction velocity. The number of grid points in the boundary layer is about 30. In the latter grid, the grid resolutions are $\Delta\xi^+ < 10$ and $\Delta\zeta^+ < 7$ near 60–90% chord length position, and $\Delta\xi^+ < 6$ and $\Delta\zeta^+ < 5$ near 80% chord length position.

Concerning boundary conditions, at the inlet boundary in cases A, C, and D the total pressure, total temperature, and flow angle shown in Tables 3 and 4 are prescribed and the static pressure is extrapolated from the interior of the calculation domain. In case B, four quantities are specified at the boundary: a Riemann invariant $R_1 = w_\perp + 2c/(\gamma - 1)$, the stagnation pressure, and the velocity components in the wall-normal and spanwise directions. The second Riemann invariant $R_2 = w_\perp - 2c/(\gamma - 1)$ is extrapolated from the interior of the calculation domain to complete the system of equations required to uniquely determine the dependent variables at the inlet. The resulting system of equations is given by

$$\begin{aligned} &w_\perp + 2c/(\gamma-1) = (w_{\perp,\infty} + w''_{\perp,1}) + 2c_\infty/(\gamma-1) \\ &w_\perp - 2c/(\gamma-1) = w_{\perp,B} - 2c_B/(\gamma-1) \qquad w_\parallel = w''_{\parallel,1} \\ &u_3 = u''_{3,1} \qquad p = P_{t,\infty}\left(1 + \frac{\gamma-1}{2}\frac{w_\perp^2 + w_\parallel^2 + u_3^2}{c^2}\right)^{-\gamma/(\gamma-1)} \end{aligned} \tag{24}$$

Here, $w''_{\perp,1}$, $w''_{\parallel,1}$, and $u''_{3,1}$ are the prescribed velocity perturbations.

At the outflow boundary, the exit static pressure shown in Table 4 is specified and the remaining variables are extrapolated from the interior of the calculation domain. It is confirmed that the reflected waves from the inlet and outlet boundaries have little influence on the pressure wave generated from the trailing edge and the boundary layer behavior for cases A, C, and D, or on the boundary layer transition for case B. The nonslip boundary condition together with an adiabatic wall condition is used on the blade wall, and periodicity is enforced in the pitchwise direction. This periodicity is imposed by a fourth-order interpolation shown below.

$$\begin{aligned} f_1 &= f_{k\max} \\ &= \frac{13(f_2 + f_{k\max-1}) + 8(f_3 + f_{k\max-2}) - 5(f_4 + f_{k\max-3})}{32} \end{aligned} \tag{25}$$

where f denotes a primitive variable, that is, density, velocity components, and static pressure. In the spanwise direction, a periodic condition is also imposed by overlapping grid points as

$$f_1 = f_{l\max-1}, \qquad f_{l\max} = f_2 \tag{26}$$

The time increment Δt was set to a constant value of $\Delta t = 2.02 \times 10^{-5} C/w_\infty$. The Courant–Friedrichs–Lewy (CFL) number, which is given by

$$\begin{aligned} \mathrm{CFL} &= \Delta t \times \max(|\tilde{U}_1| + c\sqrt{\xi_{x_i}\xi_{x_i}}, |\tilde{U}_2| + c\sqrt{\eta_{x_i}\eta_{x_i}}, |\tilde{U}_3| \\ &\quad + c\sqrt{\zeta_{x_i}\zeta_{x_i}}) \end{aligned} \tag{27}$$

is approximately 2.0. To estimate statistically averaged quantities, computational results are averaged for the time period of $1C/w_\infty$ in cases A, B, and D, and $3C/w_\infty$ in case C after the flowfields reached to a fully equilibrium state. It takes around $11C/w_\infty$ for the solution to settle into equilibrium. Time-averaged mass flows are conserved within 0.6% between the inlet and the outlet of the cascade.

Freestream turbulence added to case B must reproduce the structures of real turbulence to some extent. In the present study, freestream turbulence is obtained from an instantaneous flowfield of isotropic turbulence that was separately computed. To introduce freestream turbulence to the cascade flow, velocity fluctuations in planes with a constant separation distance are extracted from the instantaneous flowfield. After an appropriate scaling of the turbulence intensities, the resultant velocity perturbations are specified at the inlet boundary of the cascade flow through Eq. (24) at every time step.

In addition to the turbulence intensities, the integral scale is also an important parameter in freestream turbulence. In the simulation of isotropic turbulence, the initial random field that has the Kármán spectrum [36]

$$E(k) \propto \frac{\Lambda_f^5 k^4}{(1 + \Lambda_f^2 k^2)^3} \tag{28}$$

is generated where the longitudinal integral scale Λ_f is determined so that the desired integral scale can be obtained finally. In the corresponding cascade experiments, the turbulence intensity was measured, but the length scale was not. The integral scale was assumed to be one-tenth of the blade chord, that is, 10 mm, in the present LES.

Table 4 Freestream condition

Inlet	$P_{t,1}$	47,540 Pa
	$T_{t,1}$	312.9 K
Outlet	p_2	37,930 Pa

IV. Results and Discussion

A. Steady Characteristics of Compressible Transitional Cascade Flows

Concerning the steady characteristics of the compressible transitional cascade flows, computational results of cases A and B are compared with available experimental data [35]. Figure 9 compares time-averaged static pressure distribution around the blade where the pressure is nondimensionalized as

$$C_p = \frac{p - p_2}{P_{t,1} - p_2} \tag{29}$$

The computed results agree well with the experimental data. In the LES, the differences between cases A and B appear near the leading

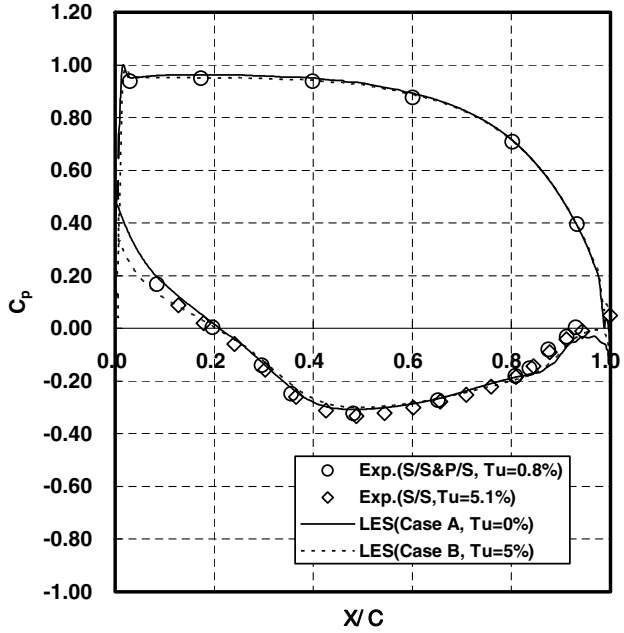

Fig. 9 Time-averaged distribution of static pressure on the blade's surface.

edge upstream of the 20% chord length position and near the trailing edge downstream of the 90% chord length position both on the suction surface. Near the leading edge, the pressure gradient of case A is steeper than that of case B, and near the trailing edge vice versa. The differences between cases A and B are attributed to the difference in the state of the boundary layer on the blade suction surface, as will be described later.

Figure 10 compares the computed time-averaged velocity profiles with experimental data measured by a pitot tube. In the figure, the results of cases C and D are also shown. Regarding the experimental data, only the data that correspond to case B are shown. The experimental data do not asymptote to zero at the wall as they should, and this seems due to inappropriateness of correction when the data were measured by the pitot probe although this problem is not discussed in [35]. With this taken into consideration, overall agreement between the present computational results and the measured data is good for case B.

Some differences between the computed results and experimental data appear at the 40 and 85% chord length positions. The difference at the 40% chord length position may partially be attributed to difficulties in resolving the thin boundary layer in the experiment where the displacement thickness and the probe height are of the same order [37]. The difference at the 85% chord length position is likely to originate from the present computational limitation to capture fast vortex breakdown in the early transition process. When case A is compared with cases C and D, respectively, the effects of a

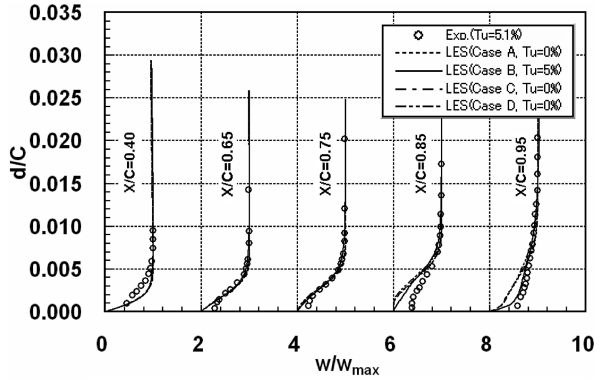

Fig. 10 Suction-side boundary layer profile at $X/C = 0.40$, 0.65, 0.75, 0.85, and 0.95.

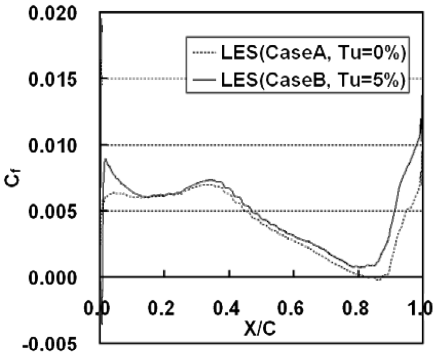

Fig. 11 Skin-friction coefficient along the suction side of the blade.

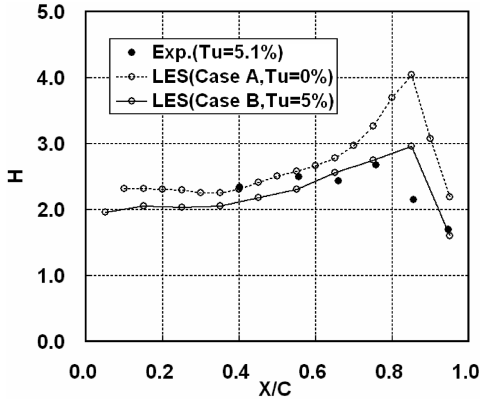

Fig. 12 Shape factor along the suction side of the blade.

longer time period of statistical average and finer grid size on the solution of case A are very small in the present computation.

On the other hand, the difference between the computational results of cases A and B appears downstream of the 85% chord length position. The computed skin-friction coefficient C_f is compared for cases A and B in Fig. 11 where the skin-friction coefficient C_f is defined as

$$C_f = \left\langle \frac{\mu_w u_{\xi,k=2}}{d_{k=2}} \right\rangle \Big/ \left(\frac{1}{2} \rho_\infty w_\infty^2 \right) \tag{30}$$

where $u_{\xi,k=2}$ is the streamwise velocity component in the first cell above the wall and $\langle\,\rangle$ denotes the spanwise and time averaging. From Figs. 10 and 11, a separation bubble is formed near the 85% chord length position in case A while the boundary layer is attached in a time-averaged sense in case B.

The computed distributions of the shape factor along the suction side of the blade are shown in Fig. 12 together with available experimental data. As is confirmed by both computational and experimental results, the boundary layer is turbulent downstream of the 95% chord length position in case B.

B. Unsteady Characteristics of Compressible Transitional Cascade Flows

In the previous section, the time-averaged characteristics of the boundary layer are discussed. In this section, unsteady characteristics of the cascade flows will be discussed. Divergence of an instantaneous velocity field is shown in Fig. 13. Here, the divergence represents the time derivative of pressure fluctuation, which is derived from the continuity equation and the definition of sound speed. In case A, pressure waves that originate from the unsteady fluctuation in the neighborhood of the trailing edge propagate in almost the entire region of the blade passage. As will be mentioned later in Fig. 22, the pressure waves oscillate the separation bubble that is formed near the 80% chord length position. Also they reach the suction side of the neighboring blade at its maximum curvature and

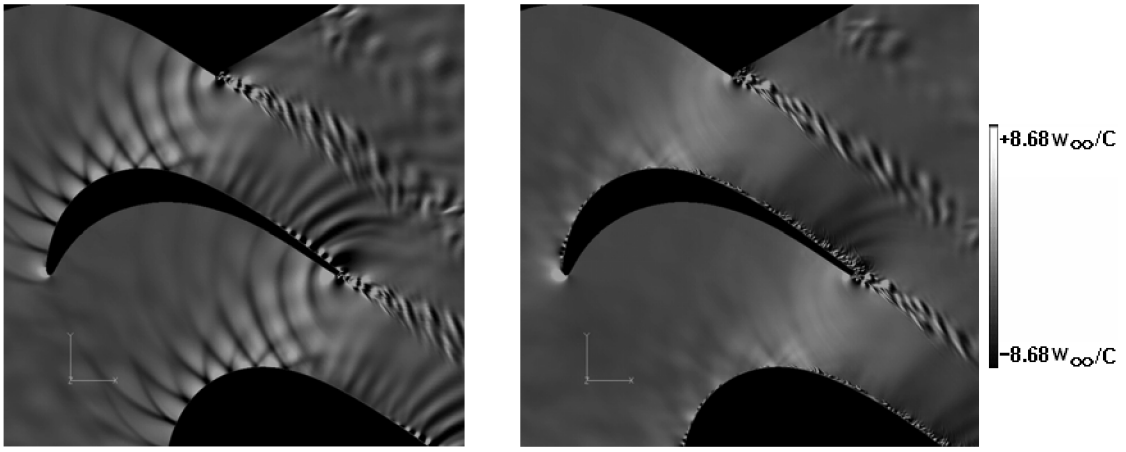

Fig. 13 Divergence of the instantaneous velocity field in the cascade (left: case A; right: case B).

form a complex pressure field upstream of the blade's throat. To the contrary, no strong periodic pressure waves are generated from the neighborhood of the trailing edge in case B. Regarding the phenomena observed in case A, the former is known as the feedback phenomena and is also found in the LES that Raverdy [5] performed for a lower Reynolds and Mach numbers than the present LES. The latter behaviors of pressure waves from the trailing edge are observed for the first time, to our knowledge. It has significance in understanding the acoustic field upstream of the cascade. The effect of vortex shedding at the trailing edge on the suction side of the neighboring blade is also mentioned in an experiment done by Sieverding et al. [38] where they measured the pressure field near the trailing edge of a transonic turbine blade with a Reynolds number of $O(10^6)$. In their experiment, however, the effect of the neighboring blade is confirmed only downstream of the throat on the suction side and the phenomena seem essentially different from what is observed in the present computation.

In Fig. 14, divergence of the instantaneous velocity field near the trailing edge is shown. In case A, pressure waves oscillate the boundary layer near the trailing edge and periodic variation of the divergence is observed. In case B, minute eddies are formed near the trailing edge. Based on these results, the qualitative change in the pressure fields in the blade passage seems closely related to the boundary layer fluctuation near the trailing edge. To confirm this, isosurface of the spanwise vorticity near the trailing edge is shown in Fig. 15. In case A, the boundary layer that retains two dimensionality convects downstream near the trailing edge and the wake also possesses two-dimensional structure, which apparently constitutes the dipole source of pressure waves. To the contrary, a fully three-dimensional turbulent boundary layer, which was confirmed by Fig. 12 and also will be reconfirmed in Fig. 21, convects downstream and the wake consists of minute three-dimensional eddies in case B. Therefore, noticeable periodic pressure waves are not generated in case B.

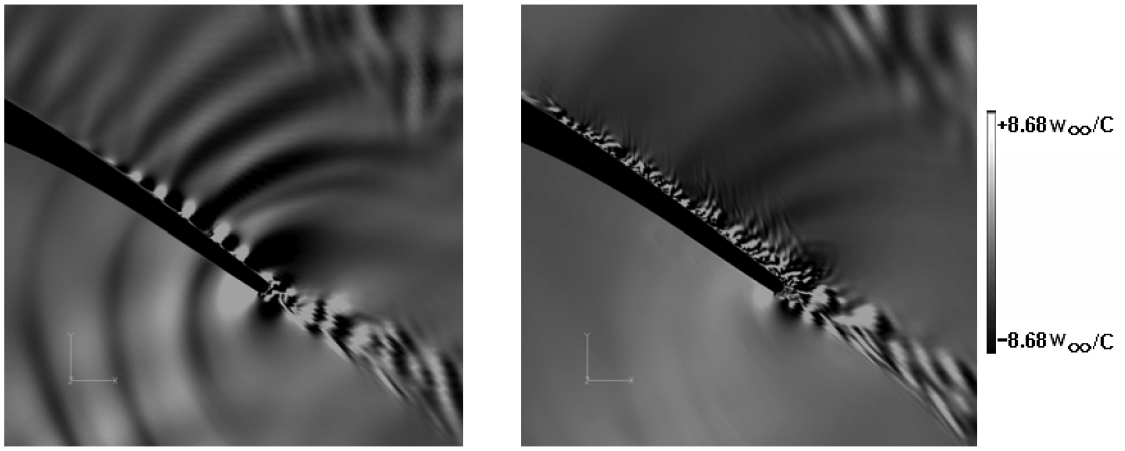

Fig. 14 Divergence of the instantaneous velocity field near the trailing edge (left: case A; right: case B).

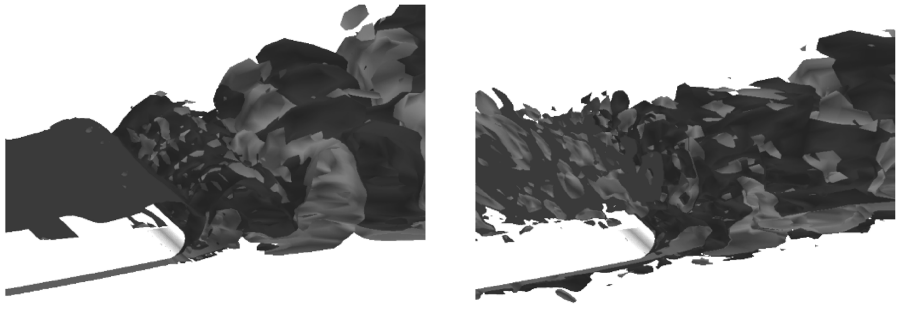

Fig. 15 Isosurface plot of the spanwise vorticity near the trailing edge at 4.34 w_∞/C (gray) and -4.34 w_∞/C (black) (left: case A; right: case B).

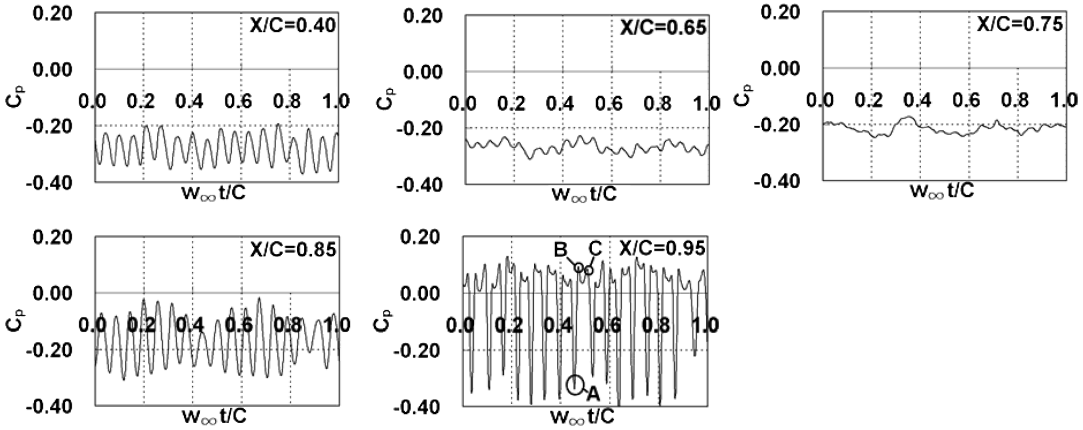

Fig. 16 Time histories of the wall surface pressure on the suction side of the blade at $X/C = 0.4, 0.65, 0.75, 0.85$, and 0.95 (case A).

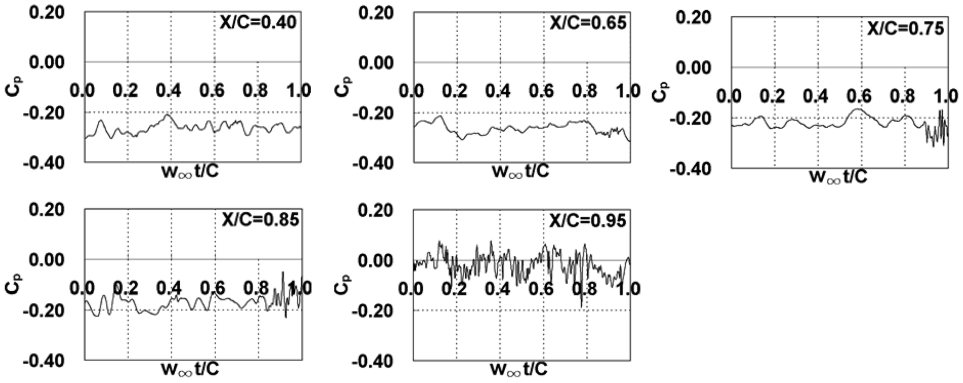

Fig. 17 Time histories of the wall surface pressure on the suction side of the blade at $X/C = 0.4, 0.65, 0.75, 0.85$, and 0.95 (case B).

Differences in the pressure fluctuations seen in the cascade also appear on the blade surface. Figures 16 and 17 show, respectively, for cases A and B, time histories of the wall surface pressure on the suction side of the blade at $X/C = 0.4, 0.65, 0.75, 0.85$, and 0.95. In case A, at the 40% chord length position the fluctuation shows a periodic variation with an amplitude of 3.5% of the time-averaged static pressure and a time period approximately of 0.067 that is nondimensionalized by the chord length and the freestream velocity at infinity upstream of the cascade. From Fig. 13, this variation is certainly attributed to the pressure wave generated from the neighboring blade. At the 65 and 75% chord length positions that are downstream of the blade's throat, the pressure fluctuation attenuates because the pressure waves generated from the trailing edge decay. At the 85% chord length position, fluctuation of the wall pressure becomes as big as approximately 5% of the time-averaged static pressure due to the pressure waves and the boundary layer separation. Furthermore, at the 95% chord length position, two peaks appear in a period of the pressure fluctuation due to the existence of the trailing edge. Here, the large pressure drop denoted as A corresponds to the point denoted as "A" in a reverse flow region in Fig. 22b that is shown later. The two peaks, that is, points B and C in the area where $C_p > 0$ originate in the separation and attachment of the boundary layer. On the other hand, no periodic variation is observed in the wall pressure fluctuations at the 40% chord length position in case B. At the 75 and 85% chord length positions, irregular high-frequency fluctuations that correspond to intermittent turbulence production, that is, turbulent spots under the influence of freestream turbulence, appear between a nondimensional time of 0.9 and 1.0. At the 95% chord length position, the boundary layer is turbulent over the period of time as was also seen in Fig. 14.

As is understood previously, differences in the state of the boundary layer due to freestream turbulence are closely related to qualitative differences in the unsteady flow. In the next subsection, it will be investigated how the growth of the boundary layer and its fluctuation are different in cases A and B.

C. Effect of Freestream Turbulence on the Growth of Boundary Layer and Its Fluctuation

Figures 18 and 19, respectively, show time histories of the fluctuations of the streamwise contravariant velocity defined in Eq. (8) and streamwise vorticity in the boundary layer at 20%δ, 60%δ, and 100%δ for case A where δ is the thickness of the boundary layer. As mentioned previously, pressure waves that originate from the unsteady fluctuation due to Kármán vortices near the trailing edge propagate in almost an entire region of the blade passage in case A. Weak fluctuations seen in the streamwise contravariant velocity as well as in the streamwise vorticity are due to the passage of the pressure waves in the cascade. Near the throat, the velocity fluctuation attenuates because the pressure waves that are generated from the trailing edge decay. At the 85 and 95% chord length positions, the fluctuations inside the boundary layer are amplified as seen in Fig. 18, which is the result of the boundary layer separation

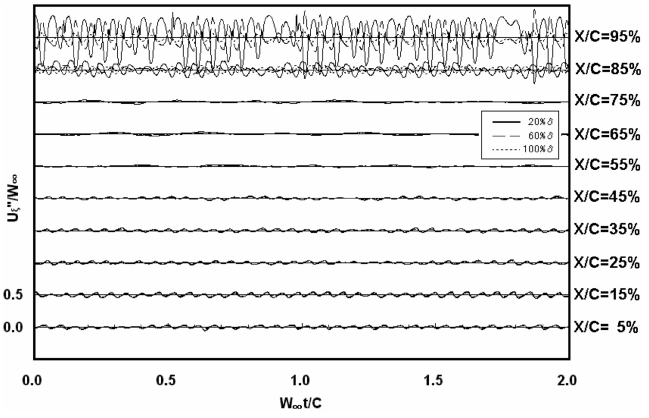

Fig. 18 Time histories of the streamwise contravariant velocity fluctuations at 20%δ, 60%δ, and 100%δ (case A).

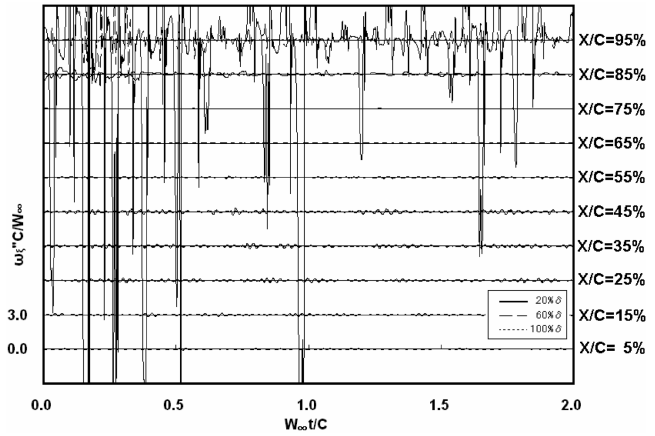

Fig. 19 Time histories of the streamwise vorticity fluctuations at 20%δ, 60%δ, and 100%δ (case A).

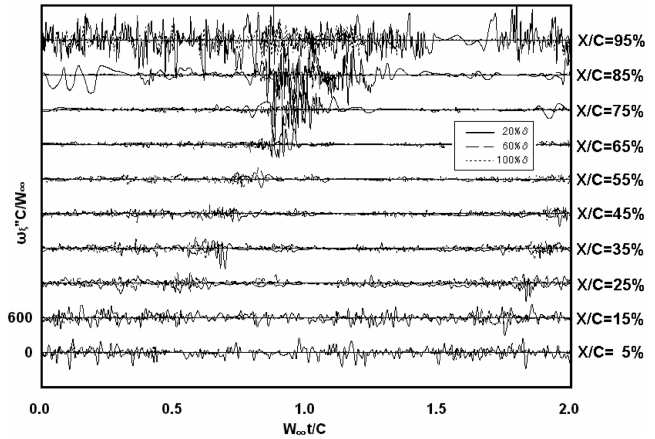

Fig. 20 Time histories of the streamwise vorticity fluctuations at 20%δ, 60%δ, and 100%δ (case B).

that takes place at the 85% chord length position. Note that at these points the phase of the fluctuations inside the boundary layer is different from that outside the boundary layer contrary to the relation observed near the leading edge. This fact means that while the pressure waves from the trailing edge propagate in an almost entire region of the blade passage, different disturbances originate in the boundary layer near the trailing edge. From the time histories of the streamwise vorticity fluctuation near the trailing edge, three-dimensional disturbances appear from the 85% chord length position.

Figure 20 shows time histories of the streamwise vorticity fluctuation at 20%δ, 60%δ, and 100%δ for case B. Near the leading edge, local separation occurs because freestream turbulence changes the incidence angle. This separation is also confirmed in Fig. 11. As a result, transition takes place and large fluctuation is observed at 20%δ of the 5% chord length position. Downstream of the leading edge, this fluctuation monotonously decreases until the midchord position ($X/C = 0.55$) where it starts to increase again as is confirmed from the frequency spectra of the streamwise contravariant velocity shown in Fig. 21. At the 75 and 85% chord length positions, strong disturbance is again observed in a time period of 0.8–1.2 $w_\infty t/C$ at 20%δ. At the 95% chord length position, disturbances larger than those of freestream turbulence occur in the entire time period.

To further investigate differences between cases A and B observed in the velocity and vorticity fluctuations, the vortical structures inside the boundary layer on the suction side are visualized. Figure 22a shows an isosurface of the second invariance of the velocity gradient tensor and divergence of the instantaneous velocity field at the same instance. Here, the second invariance Q_{inv} is defined as $Q_{\text{inv}} = -(S_{ij}S_{ij} - W_{ij}W_{ij})/2$ where S_{ij} and W_{ij} are the symmetric and asymmetric parts of the velocity gradient tensor $A_{ij} = (\partial_j u_i)$. The region where $Q_{\text{inv}} > 0$ represents vortical structures. Spanwise vorticities are created due to the boundary layer separation near the 85% chord length position and they are convected downstream while causing the velocity fluctuation. Figure 22b shows divergence of the instantaneous velocity field and velocity vectors near $X/C = 0.85$ at the same instance as Fig. 22a. Concerning the relationship between the vortical structure near the trailing edge and the pressure waves from the trailing edge, the peaks of the divergence are formed in front of and behind each vortex.

In Fig. 23a, contour of the vorticity magnitude on the blade suction surface is shown for case B. Streaky structures of vorticity, which are the characteristics of the boundary layer transition subjected to freestream turbulence, are observed near the throat where disturbances decay inside the boundary layer as was seen in Fig. 21. Near the 85% chord length position where intermittent strong disturbance takes place inside the boundary layer, burst with reverse flow occurs as seen in Fig. 23b. At the 95% chord length position, the region with a strong vorticity extends in the spanwise direction and a turbulent boundary layer develops as is confirmed by the formation of the inertial subrange with $-5/3$ power slope of Fig. 21 and by the shape factor of $H \approx 1.5$ (Fig. 12). Figure 24 presents growth of $u_{\xi,\text{rms}}$ along the suction surface downstream of the throat for case B. Here the abscissa is nondimensionalized by the local displacement thickness and the ordinate by the freestream velocity. For reference, Fig. 25 shows growth of u_{rms} measured in experiment [39] of a flat plate boundary layer that is subjected to freestream disturbances and results in a bypass transition [39]. In this experiment after the amplification of the streamwise velocity fluctuation near the wall to the level approximately of 10%, breakdown of streaks occurs and turbulent boundary layer emerges. In the present simulation, the fluctuation near the wall grows up to approximately 15% of the velocity at the edge of the boundary layer, which qualitatively agrees with the aforementioned experimental observation.

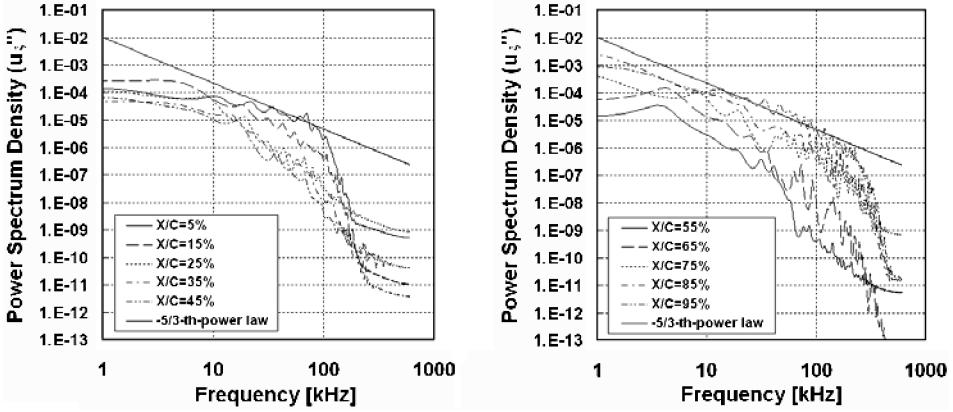

Fig. 21 Frequency spectra of streamwise contravariant velocity fluctuations at 20%δ of X/C = 5–95% (case B) (left: from 5 to 45%; right: from 55 to 95%).

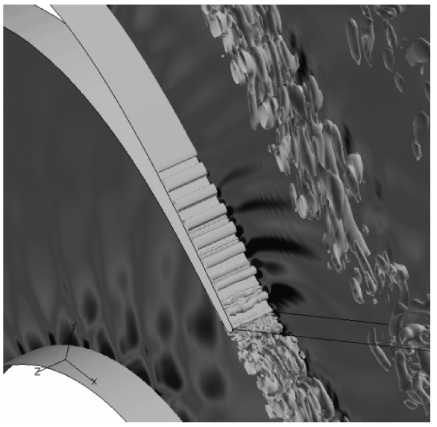

a) Iso-surface of 2nd invariance

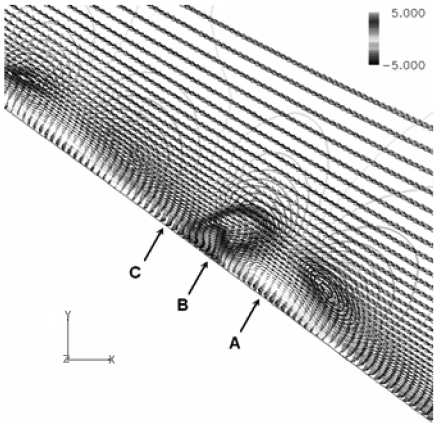

b) Divergence of instantaneous velocity field and velocity vectors near X/C=0.85

Fig. 22 Instantaneous boundary layer structures on suction surface (case A).

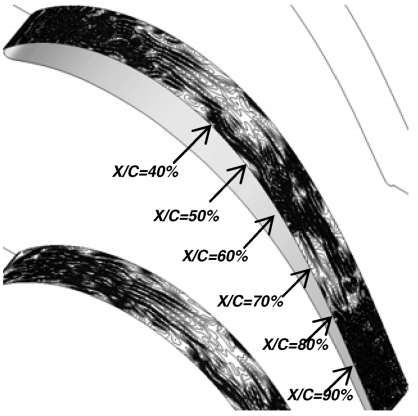

a) contour of |ω|

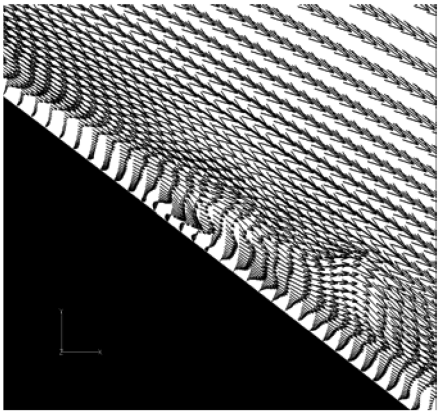

b) Velocity vectors near X/C=0.85

Fig. 23 Instantaneous boundary layer structures on suction surface (case B).

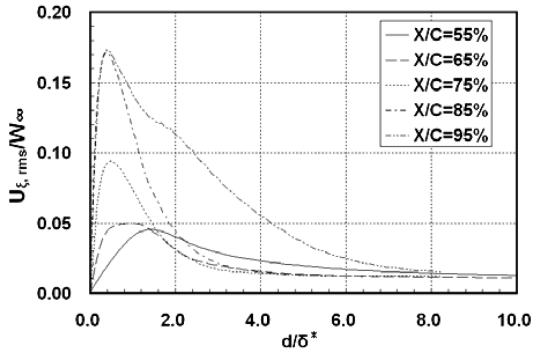

Fig. 24 Growth of $u_{\xi,\mathrm{rms}}$ along blade suction surface (case B).

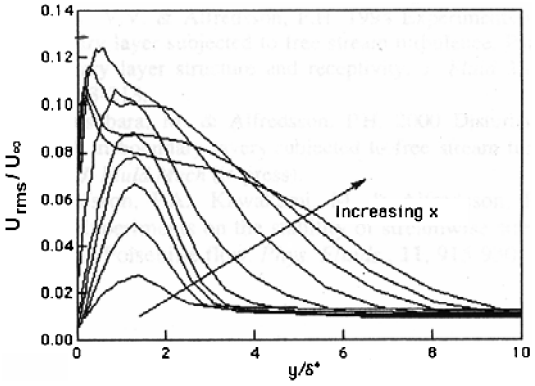

Fig. 25 Growth of u_{rms} in a flat plate boundary layer subjected to freestream disturbance [39].

Regarding the differences between cases A and B, the effects of freestream turbulence on the boundary layer separation are also important. As was seen in Fig. 11 the minimal value of the skin-friction coefficient C_f does not become negative in case B, meaning that the boundary layer near the trailing edge is attached in a time-averaged sense. For a lower Reynolds number, similar results are shown in the DNS of Kalitzin et al. [7] where they introduced isotropic freestream turbulence of 5% at the inlet. Regarding the reason why the time-averaged skin-friction coefficient is positive in case B, two possibilities can be considered. One is that separation bubbles are not formed due to the strong freestream turbulence and therefore, an attached transitional boundary layer is formed. The other possibility is that separation bubbles are formed but in an intermittent manner and the skin-friction coefficient takes a positive value in the time average. To verify these possibilities, time histories of the streamwise contravariant velocity on the suction side of the blade are plotted for case B in Fig. 26.

These streamwise contravariant velocities are sampled at the second grid point above the suction surface, and the distance from the wall based on the wall unit is written in the parentheses. All the sampling points are within the viscous sublayer ($d^+ < 5$).

First, attention is paid to the velocity fluctuations from a nondimensional time of 0–0.8. As the position goes downstream from the 60% chord length position, velocity gradually decreases from $0.05w_\infty$ and becomes negative at the 75 and 80% chord length positions. At the 85 and 90% chord length positions, the fluctuation is

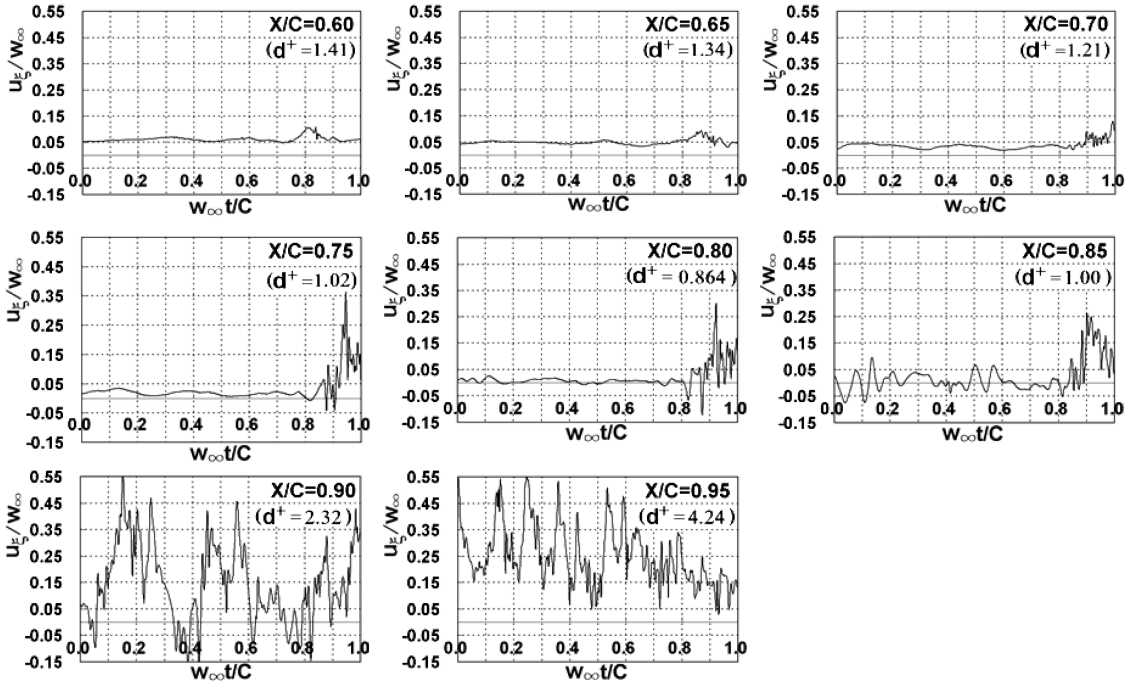

Fig. 26 Time histories of the streamwise contravariant velocity on the suction side of the blade at $X/C = 0.6, 0.65, 0.70, 0.75, 0.80, 0.85, 0.90$, and 0.95 (case B).

amplified further and the negative peak reaches $-0.15w_\infty$ at its minimum. At the 95% chord length position, the velocity becomes positive again at the entire period of time. Based on the above discussion, intermittent separation in the boundary layer takes place, which makes the time average C_f become positive.

Then, attention is paid to the high-frequency velocity fluctuation that appears from the nondimensional time of 0.8–1.0. The fluctuation that appears about the nondimensional time of 0.8 at the 60% chord length position propagates to the 75% chord length position while growing rapidly. This fluctuation, which corresponds to turbulent spots as mentioned in Fig. 20, is noticeable up to the 85% chord length position. After the 90% chord length position, this type of intermittent fluctuation is not recognizable.

When transitional separated flows are affected by strong freestream turbulence, the processes of bypass transition and separated-flow transition are reported to coexist in experiments [40,41] and DNS [9]. With this taken into consideration, the transition process of unsteady separated flow and the formation of turbulent spots under the freestream turbulence seem to coexist in the present computation.

D. Dominant Unsteady Behavior of Transitional Boundary Layer

To extract dominant unsteady behaviors of the transitional boundary layer, POD analysis is performed. The method used in the present study is Sirovich's snapshot POD method [11]. By using this method, the streamwise velocity fluctuation is orthogonally decomposed based on M instantaneous snapshots of the flowfield near the trailing edge. The domain extends from the 60% chord length position to the 100% chord length position, and from the wall surface to more than twice the boundary layer thickness in the streamwise and wall-normal directions, respectively. The spanwise extent of the domain is the same with the computational grid shown in Fig. 8. In the method, fluctuation $\boldsymbol{u}''_\xi(\boldsymbol{x}, t)$ is expanded by a set of eigenfunctions $\{\boldsymbol{\phi}_i(\boldsymbol{x})\}_{i=1}^M$ and the corresponding coefficients $\{a_i(t)\}_{i=1}^M$ as

$$\boldsymbol{u}''_\xi(\boldsymbol{x}, t) = \sum_{i=1}^{M} a_i(t)\boldsymbol{\phi}_i(\boldsymbol{x}) \tag{31}$$

Here, $\boldsymbol{u}''_\xi(\boldsymbol{x}, t)$ and $\boldsymbol{\phi}_i(\boldsymbol{x})$ are N-dimensional vectors of position with a single coordinate, N is the total number of grid points that consist of an instantaneous flowfield, that is,

$$N = j\max \times k\max \times l\max \tag{32}$$

In the present study, 1000 snapshots of the flowfield near the trailing edge are collected with a time step of 50 intervals for the analysis, that is, $M = 1000$. Eigenfunction $\boldsymbol{\phi}_i(\boldsymbol{x})$ is obtained by the algebraic equation shown below.

$$\boldsymbol{C}\,\boldsymbol{f}_i = \lambda_i \boldsymbol{f}_i \tag{33}$$

Here, $\boldsymbol{C} = (C_{m,n})$ is a $M \times M$ matrix, λ_i is an eigenvalue, and $\boldsymbol{f}_i = (f_{m,i})$ is an eigenvector. The elements of $C_{m,n}$ are defined as

$$C_{m,n} = \langle \boldsymbol{u}''_\xi(\boldsymbol{x}, t_m), \boldsymbol{u}''_\xi(\boldsymbol{x}, t_n)\rangle, \qquad m, n \in (1, \ldots, M) \tag{34}$$

where $\langle\cdot,\cdot\rangle$ is the Euclidean inner product. The above eigenvectors are scaled such that

$$\|\boldsymbol{f}_i\|^2 = \sum_{k=1}^{M} f_{k,i}^2 = \lambda_i, \qquad i \in (1, \ldots, M) \tag{35}$$

Then, the eigenvector $\boldsymbol{\phi}_i(\boldsymbol{x})$ is defined as

$$\boldsymbol{\phi}_i(\boldsymbol{x}) = \frac{1}{\lambda_i}\sum_{k=1}^{M} f_{k,i}\boldsymbol{u}''_\xi(\boldsymbol{x}, t_k) \tag{36}$$

The eigenvector $\boldsymbol{\phi}_i(\boldsymbol{x})$ has a property such that

$$\boldsymbol{\phi}_k(\boldsymbol{x}) \cdot \boldsymbol{\phi}_l(\boldsymbol{x}) = \delta_{kl}, \qquad k, l \in (1, \ldots, M) \tag{37}$$

where $\delta_{k,l}$ is Kronecker's delta function. Using the orthogonality of $\boldsymbol{\phi}_k(\boldsymbol{x})$, the coefficient $a_i(t)$ is derived as

$$a_i(t) = \boldsymbol{\phi}_i(\boldsymbol{x}) \cdot \boldsymbol{u}''_\xi(\boldsymbol{x}, t)^t \tag{38}$$

In Fig. 27, the fractional energy of the first 10 dominant POD modes is plotted. In case A, there are two dominant modes in which the first eigenvalue accounts for the fractional energy of 36.1%, the second eigenvalue 35.1%. In case B, there is one dominant mode, which accounts for the fractional energy of 28.5%. In Fig. 28, time histories of the four dominant POD modes' coefficients for cases A and B are shown. In case A, the first and second modes always appear

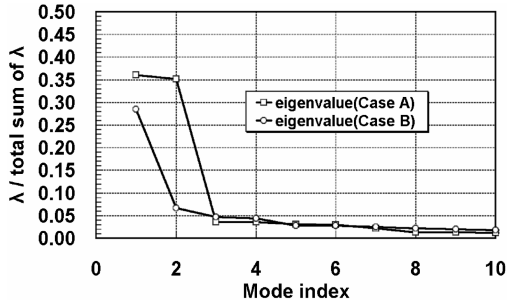

Fig. 27 Fractional energy of the first 10 dominant POD modes.

more remarkably than the third and fourth modes. In case B, the absolute value of the coefficient of the first mode increases rapidly between the nondimensional time of 0.8–1.0 and it becomes the most dominant in this time period while in the other period of time the other modes are dominant. In case B, as is shown in Fig. 20, the noticeable turbulence production occurs near the trailing edge between the nondimensional time of 0.8 and 1.0. Therefore, the first mode is thought to have a close relationship with the intermittent turbulence production.

Based on the aforementioned eigenfunctions and the coefficients, the streamwise contravariant velocity fluctuation is reconstructed. Figure 29 shows accumulated plots of instantaneous velocity fluctuation profiles at the 85% and the 95% chord length positions and the component reconstructed from the two dominant POD modes for case A. Here, the abscissa is the distance from the wall. The region swept by the profiles of the component reconstructed from the first mode has symmetry regarding the abscissa both at the 85 and 95% chord length positions. The change of sign in the instantaneous velocity fluctuation profiles is also confirmed around $d/C = 0.005$. Near the trailing edge the spanwise vortices are created, and each vortex is accompanied by a reverse flow region as shown in Fig. 22. With the correspondence between this profile and the vortical structure taken into consideration, the passage of the periodic vortex is the dominant behavior of the boundary layer near the trailing edge. Intuitively, if we focus on the region where $d/C < 0.005$, the above symmetry means that the amplitude of the largest velocity fluctuation in the reverse flow region is almost equal to that in the accelerating flow region in terms of the first mode. On the other hand, at the 85% chord length position, the region swept by the profiles of the second mode is much smaller than those of the first mode, and at the 95% chord length position, the former becomes larger than the latter. At the 95% chord length position, the sign of the second mode changes at a point farther apart from the wall than the first mode. In Fig. 22, the vortices near the trailing edge are compressed and expanded by the passage of pressure waves as is found in the relationship between the divergence values and the vortices. Therefore, the difference in the position where the sign changes in the first mode and the second mode corresponds to the compression and expansion of the vortices. Furthermore, the region swept by the profiles of the second mode has asymmetry regarding the abscissa. This asymmetry means that large velocity fluctuations sometimes occur in the accelerating flow region compared to the reverse flow region in terms of the second mode, and therefore, corresponds to the deformation of the spanwise vorticies in the spanwise direction near the trailing edge as is found in Fig. 22.

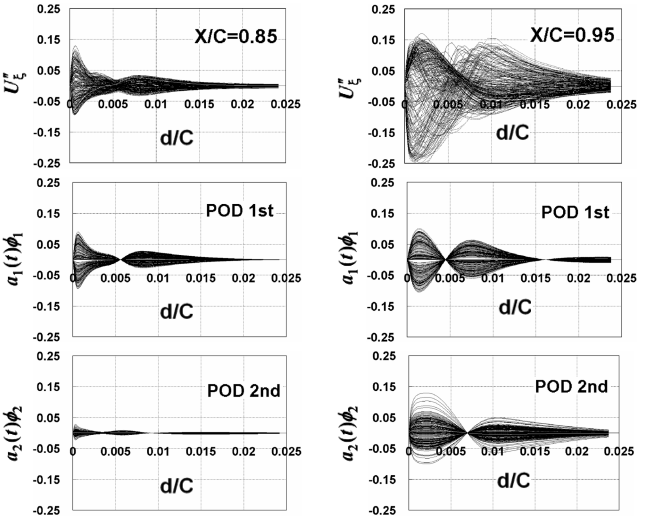

Fig. 29 Accumulated plots of instantaneous velocity profiles at $X/C =$ 0.85 and 0.95, and instantaneous velocity component reconstructed from the two dominant POD modes (case A).

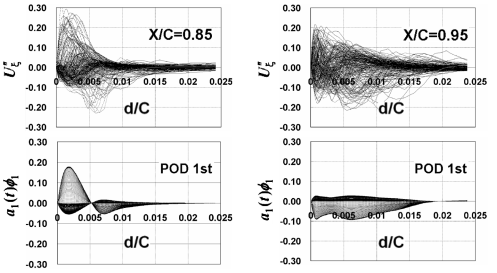

Fig. 30 Accumulated plots of instantaneous velocity profiles at $X/C =$ 0.85 and 0.95, and instantaneous velocity component reconstructed from the one dominant POD mode (case B).

Based on the above discussion, in addition to the passage of periodic vortices, the compression and expansion of vortices due to the passage of the pressure waves are the dominant behavior of the boundary layer in the no freestream turbulence case. Especially at the 95% chord length position, the spanwise deformation of vortices is also the dominant unsteady behavior of the transitional boundary layer.

Figure 30 shows accumulated plots of instantaneous velocity fluctuation profiles at the 85 and 95% chord length positions, and the component reconstructed from the most dominant POD mode for case B. In this case, due to freestream turbulence, the characteristic velocity fluctuation mentioned also in Fig. 24 occurs near the wall, and this fluctuation is the dominant behavior of the boundary layer from the region swept by the first mode. At the 95% chord length position, a large fluctuation is observed both near the wall and $d/C = 0.005$ far from the wall. In the region swept by the profiles reconstructed by the first mode, two peaks are confirmed. To understand the physical meaning of these two peaks, the budget equation for the turbulent kinetic energy in a compressible turbulent boundary layer [42] is analyzed. In the equation, turbulent

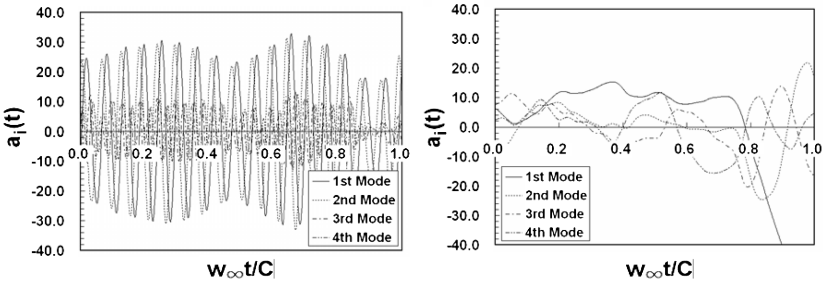

Fig. 28 Time histories of the four dominant POD modes' coefficient (left: case A; right: case B).

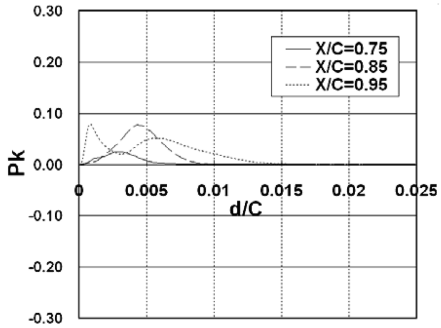

Fig. 31 Plot of turbulence production at $X/C = 75$, 85, and 95% (case B).

production P_k is defined as

$$P_k = -\bar{\rho}\,\widetilde{u_i'u_k'}\,\frac{\partial \tilde{u}_i}{\partial x_k} \tag{39}$$

In Fig. 31, turbulence productions are plotted at the 75, 85, and 95% chord length positions for case B. The peak of turbulence production at $d/C \approx 0.0025$ of the 75% chord length position is also confirmed at $d/C \approx 0.005$ of the 85% chord length position. The distance from the wall at the 85% chord length position corresponds to the node of the region by the first mode in Fig. 30, and therefore, the peak of turbulence production is due to the velocity shear. At the 95% chord length position, the peak at $d/C \approx 0.005$ also originates from the same event. On the other hand, regarding the production at $d/C \approx 0.0008$, it is due to the development of the turbulent boundary layer near the wall with the shape factor in Fig. 12 also taken into consideration. The region swept by the profiles reconstructed by the first mode has a similar shape to the turbulence production. Therefore, in case B the growth of the streamwise velocity fluctuation and the production of turbulent kinetic energy are the dominant behaviors of the transitional boundary layer at the 85 and 95% chord length positions, respectively. Based on the above discussions, the dominant behavior of the transitional boundary layer is intrinsically different in cases A and B.

V. Conclusions

Large-eddy simulation of compressible transitional flows in a low-pressure turbine cascade is performed by using the sixth-order compact difference and a 10th-order filtering method. Numerical results without freestream turbulence and those with approximately 5% freestream turbulence are compared. Based on the computed results, differences in the unsteady behaviors of flows in the cascade, including the propagation of pressure waves and the effect of freestream turbulence on separated flows, are discussed. In addition, POD analysis is performed to extract the dominant behaviors of the unsteady boundary layers.

Separated flows in the turbine cascade accompanied by laminar-turbulent transition are realized, and the present results closely agree with past experimental measurements in terms of the static pressure distribution around the blade.

In the case where no freestream turbulence is taken into account, the pressure waves give unsteady fluctuations on the separation bubble near the trailing edge. Also, they reach the region of maximum curvature on the suction side of the neighboring blade and form a complex pressure field even upstream of the throat. On the other hand, in the case where 5% of freestream turbulence is taken into account, the generation of periodic pressure waves in the neighborhood of the trailing edge becomes weak and hardly recognizable. Therefore, the unsteady pressure field is essentially altered by the existence of strong freestream turbulence.

When transitional separated flow is subjected to strong freestream turbulence, formation of the separation bubble becomes highly unsteady and the statistically averaged skin-friction coefficient becomes positive in a time-averaged sense.

In the no freestream turbulence case, in addition to the convection of periodic vortices, the compression and expansion of vortices due to the passage of the pressure waves are found to become the dominant behaviors of the boundary layer from the two dominant POD modes that account for the fractional energy of more than 30%. Especially at the 95% chord length position, the deformation of the vortices in the spanwise direction also appears and it also becomes the dominant unsteady behavior of the transitional boundary layer for the no freestream turbulence case. When freestream turbulence is taken into account, the growth of the streamwise velocity fluctuation and the production of turbulent kinetic energy are found to become the dominant behavior of the transitional boundary layer at the 85 and 95% chord length positions, respectively. Based on the above discussions, it is found that the dominant unsteady behaviors of the transitional boundary layer are essentially different in with and without freestream turbulence cases.

Acknowledgments

This research has been supported by a 21st century COE program "Mechanical System Innovation" of the University of Tokyo. The authors would also like to thank the Information Technology (IT) research program "Frontier Simulation Software for Industrial Science" supported by the Ministry of Education, Culture, Sports, Science and Technology (MEXT), and a collaborative research project with Japan Aerospace Exploration Agency (JAXA) "Simulation of Internal Flows in Rocket Engines," both of which provided computational resources needed to pursue this research.

References

[1] Mayle, R. E., "The Role of Laminar-Turbulent Transition in Gas Turbine Engines," *Journal of Turbomachinery*, Vol. 113, No. 4, 1991, pp. 509–537.

[2] Matsunuma, T., Ph.D. Dissertation, Department of Mechanical Engineering, University of Tokyo, 2003 (in Japanese).

[3] Emmons, H. W., "The Laminar-Turbulent Transition in a Boundary Layer-Part 1," *Journal of the Aeronautical Sciences*, Vol. 18, No. 7, 1951, pp. 490–498.

[4] Mittal, R., Venkatasubramanian, S., and Najjar, F. M., "Large-Eddy Simulation of Flow Through a Low-Pressure Turbine Cascade," AIAA Paper 2001-2560, 2001.

[5] Raverdy, B., Mary, I., and Sagaut, P., "High-Resolution Large-Eddy Simulation of Flow Around Low-Pressure Turbine Blade," *AIAA Journal*, Vol. 41, No. 3, 2003, pp. 390–397.

[6] Wu, X., and Durbin, P. A., "Evidence of Longitudinal Vortices Evolved from Distorted Wakes in a Turbine Passage," *Journal of Fluid Mechanics*, Vol. 446, 2001, pp. 199–228.

[7] Kalitzin, G., Wu, X., and Durbin, P. A., "DNS of Fully Turbulent Flow in a LPT Passage," *International Journal of Heat and Fluid Flow*, Vol. 24, No. 4, 2003, pp. 636–644.

[8] Wissink, J. G., "DNS of Separating, Low Reynolds Number Flow in a Turbine Cascade with Incoming Wakes," *International Journal of Heat and Fluid Flow*, Vol. 24, No. 4, 2003, pp. 626–635.

[9] Michelassi, V., Wissink, J. G., Fröhlich, J., and Rodi, W., "Large-Eddy Simulation of Flow Around Low-Pressure Turbine Blade with Incoming Wakes," *AIAA Journal*, Vol. 41, No. 11, 2003, pp. 2143–2156.

[10] Matsuura, K., "Large Eddy Simulation of Compressible Transitional Cascade Flows," *Transactions of the Japan Society of Mechanical Engineers*, Vol. 70, No. 700B, 2004, pp. 3066–3073 (in Japanese).

[11] Sirovich, L., and Rodriguez, J. D., "Coherent Structures and Chaos: A Model Problem," *Physics Letters A*, Vol. 120, No. 5, 1987, pp. 211–214.

[12] Vreman, B., Geurts, B., and Kuerten, H., "A Priori Tests of Large Eddy Simulation of the Compressible Plane Mixing Layer," *Journal of Engineering Mathematics*, Vol. 29, No. 4, 1995, pp. 299–327.

[13] Vreman, B., Geurts, B., and Kuerten, H., "Subgrid-Modelling in LES of Compressible Flow," *Applied Scientific Research*, Vol. 54, No. 3, 1995, pp. 191–203.

[14] Speziale, C. G., Erlebacher, G., and Zang, T. A., "The Subgrid-Scale Modeling of Compressible Turbulence," Brief Communication, *Physics of Fluids A*, Vol. 31, No. 4, 1988, pp. 940–942.

[15] Erlebacher, G., Hussaini, M. Y., Speziale, C. G., and Zang, T. A., "Toward the Large-Eddy Simulation of Compressible Turbulent Flows," *Journal of Fluid Mechanics*, Vol. 238, 1992, pp. 155–185.

[16] Moin, P., Squires, K., Cabot, W., and Lee, S., "A Dynamic Subgrid-Scale Model for Compressible Turbulence and Scalar Transport," *Physics of Fluids A*, Vol. 3, No. 11, 1991, pp. 2746–2757.
[17] Boris, J. P., Grinstein, F. F., Oran, E. S., and Kolbe, R. L., "New Insights into Large Eddy Simulation," *Fluid Dynamics Research*, Vol. 10, Nos. 4–6, 1992, pp. 199–288.
[18] Visbal, M. R., and Rizzetta, D. P., "Large-Eddy Simulation on Curvilinear Grids Using Compact Differencing and Filtering Schemes," *Journal of Fluids Engineering*, Vol. 124, No. 4, 2002, pp. 836–847.
[19] Smagorinsky, J., "General Circulation Experiments with the Primitive Equations," *Monthly Weather Review*, Vol. 91, No. 3, 1963, pp. 99–164.
[20] Germano, M., Piomelli, U., Moin, P., and Cabot, W., "A Dynamic Subgrid-Scale Eddy-Viscosity Model," *Physics of Fluids A*, Vol. 3, No. 7, 1991, pp. 1760–1765.
[21] Van Driest, E. R., "On Turbulent Flow Near a Wall," *Journal of the Aeronautical Sciences*, Vol. 23, No. 11, 1956, pp. 1007–1011.
[22] Lele, S. K., "Compact Finite Difference Schemes with Spectral-Like Resolution," *Journal of Computational Physics*, Vol. 103, No. 1, 1992, pp. 16–42.
[23] Beam, R., and Warming, R., "An Implicit Factored Scheme for the Compressible Navier-Stokes Equations," *AIAA Journal*, Vol. 16, No. 4, 1978, pp. 393–402.
[24] Pulliam, T. H., and Chaussee, D. S., "Diagonal Form of an Implicit Approximate-Factorization Algorithm," *Journal of Computational Physics*, Vol. 39, No. 2, 1981, pp. 347–363.
[25] Pulliam, T. H., "Artificial Dissipation Models for the Euler Equations," *AIAA Journal*, Vol. 24, No. 12, 1986, pp. 1931–1940.
[26] Carpenter, M. H., Gottlieb, D., and Abarbanel, S., "The Stability of Numerical Boundary Treatments for Compact High-Order Finite-Difference Schemes," *Journal of Computational Physics*, Vol. 108, No. 2, 1993, pp. 272–295.
[27] Kravchenko, A. G., and Moin, P., "On the Effect of Numerical Errors in Large Eddy Simulations of Turbulent Flows," *Journal of Computational Physics*, Vol. 131, No. 2, 1997, pp. 310–322.
[28] Gaitonde, D. V., and Visbal, M. R., "Padé-Type Higher-Order Boundary Filters for the Navier-Stokes Equations," *AIAA Journal*, Vol. 38, No. 11, 2000, pp. 2103–2112.
[29] Matsuura, K., Ph.D. Dissertation, Department of Mechanical Engineering, University of Tokyo, 2005 (in Japanese).
[30] Naik, N. H., Naik, V. K., and Nicoules, M. N., "Parallelization of a Class of Implicit Finite Difference Schemes in Computational Fluid Dynamics," *International Journal of High Speed Computing*, Vol. 5, No. 1, 1993, pp. 1–50.
[31] Pironneau, O., Rodi, W., Ryhming, I. L., Savill, A. M., and Truong, T. V., "Numerical Simulation of Unsteady Flows and Transition to Turbulence," *Proceedings of the ERCOFTAC Workshop*, Cambridge Univ. Press, Cambridge, U.K., 1990.
[32] Voke, P., "Subgrid-Scale Modelling at Low Mesh Reynolds Number," *Theoretical and Computational Fluid Dynamics*, Vol. 8, No. 2, 1996, pp. 131–143.
[33] Poinsot, T. J., and Lele, S. K., "Boundary Conditions for Direct Simulations of Compressible Viscous Flows," *Journal of Computational Physics*, Vol. 101, No. 1, 1992, pp. 104–129.
[34] Jacobs, R. G., and Durbin, P. A., "Simulation of Bypass Transition," *Journal of Fluid Mechanics*, Vol. 428, 2001, pp. 185–212.
[35] Fottner, L. (ed.), "Test Cases for Computation of Internal Flows in Aero Engine Components," AGARD, AR-275, 1990, pp. 112–123.
[36] Hinze, J. O., *Turbulence*, McGraw–Hill, New York, 1975.
[37] Hoheisel, H., Kiock, R., Lichtfuss, H. J., and Fottner, L., "Influence of Free-Stream Turbulence and Blade Pressure Gradient on Boundary Layer and Loss Behavior of Turbine Cascades," *Journal of Turbomachinery*, Vol. 109, No. 2, 1987, pp. 210–219.
[38] Sieverding, C. H., Richard, H., and Desse, J., "Turbine Blade Trailing Edge Flow Characteristics at High Subsonic Outlet Mach Number," *Journal of Turbomachinery*, Vol. 125, No. 2, 2003, pp. 298–309.
[39] Alfredsson, P. H., and Matsubara, M., "Free-Stream Turbulence, Streaky Structures and Transition in Boundary Layer Flows," AIAA Paper 2000-2534, 2000.
[40] Volino, R. J., and Hultgren, L. S., "Measurements in Separated and Transitional Boundary Layers Under Low-Pressure Turbine Airfoil Conditions," *Journal of Turbomachinery*, Vol. 123, No. 2, 2001, pp. 189–197.
[41] Volino, R. J., "Separated Flow Transition Under Simulated Low-Pressure Turbine Airfoil Conditions-Part 2: Turbulence Spectra," *Journal of Turbomachinery*, Vol. 124, No. 4, 2002, pp. 656–664.
[42] Huang, P. G., Coleman, G. N., and Bradshaw, P., "Compressible Turbulent Channel Flow: DNS Results and Modelling," *Journal of Fluid Mechanics*, Vol. 305, 1995, pp. 185–218.

R. So
Associate Editor